Global Flash Drought Monitoring using Surface Soil Moisture

Vinit Sehgal[1], Nandita Gaur[2,3], Binayak P. Mohanty[3]

[1]Water Management and Hydrological Science, Texas A& M University, TX 77843, USA

[2]Now at Department of Crop and Soil Sciences, University of Georgia, Athens, GA 30602, USA.

[3]Biological and Agricultural Engineering, Texas A&M University, TX 77843, USA.

Key Points:

- A new method for near-real-time global flash drought monitoring with SMAP soil moisture and footprint-scale drydown parameters
- Flash drought mechanism is evaluated using soil moisture state (stress) and rate of soil moisture drydown (intensification)
- Global index correlates with 1-month meteorological anomalies and shows high skill in forecasting vegetation health with 0-2 weeks lead

Keywords: Flash drought; SMAP satellite; Soil moisture; Drought monitoring; Soil moisture drydown

Corresponding author: Binayak P. Mohanty, `bmohanty@tamu.edu`

Abstract

Flash droughts are characterized by an abrupt onset and swift intensification. Global surface soil moisture (θ_{RS}) from NASA's Soil Moisture Active Passive (SMAP) satellite can facilitate a near-real-time assessment of emerging flash droughts at 36-km footprint. However, a robust flash drought monitoring using θ_{RS} must account for the i) short observation record of SMAP, ii) non-linear geophysical controls over θ_{RS} dynamics, and, iii) emergent meteorological drivers of flash droughts. We propose a new method for near-real-time characterization of droughts using Soil Moisture Stress (SMS, drought stress) and Relative Rate of Drydown (RRD, drought stress intensification rate) — developed using SMAP θ_{RS} (March 2015-2019) and footprint-scale seasonal soil water retention parameters and land-atmospheric coupling strength. SMS and RRD are nonlinearly combined to develop Flash Drought Stress Index (FDSI) to characterize emerging flash droughts (FDSI $\geq$ 0.71 for moderate to high RRD and SMS). Globally, FDSI shows high correlation with concurrent meteorological anomalies. A retrospective evaluation of select droughts is demonstrated using FDSI, including a mechanistic evaluation of the 2017 flash drought in the Northern Great Plains. About 5.2% of earth's landmass experienced flash droughts of varying intensity and duration during 2015-2019 (FDSI $\geq$ 0.71 for >30 consecutive days), majorly in global drylands. FDSI shows high skill in forecasting vegetation health with a lead of 0-2 weeks, with exceptions in irrigated croplands and mixed forests. With readily available parameters, low data latency, and no dependence on model simulations, we provide a robust tool for global near-real-time flash drought monitoring using SMAP.

1 Introduction

Flash droughts are characterized by three S's: Speed, Severity and Spread, i.e., rapid intensification of drought to severe levels over a large area (Christian et al., 2019; Otkin et al., 2017). These fast-evolving droughts are associated with large-scale agricultural losses (Jencso et al., 2019; Jin et al., 2019), expansive wildfires (Christian et al., 2020) and potential challenges for seasonal and sub-seasonal climate predictions (Pendergrass et al., 2020). The frequency and intensity of flash droughts are reported to be on the rise (Touma et al., 2015; Yuan et al., 2019), accompanied by a global increase in the drought recovery period (Schwalm et al., 2017). Hence, near-real-time identification and early-warning of flash droughts have implications for global food and water security.

Flash droughts are triggered by anomalously high temperatures (heatwave flash drought) or lack of precipitation (precipitation-deficit flash droughts) (Christian et al., 2019; Otkin et al., 2017), however, a rapid decrease of soil moisture (SM) is common to the development of both types of flash droughts (Liu et al., 2020; Mo & Lettenmaier, 2015, 2016). NASA's Soil Moisture Active Passive (SMAP) satellite provides global observations of SM, termed θ_{RS}, at 36-km footprint with minimal error (within $\pm$ 0.04 m^3/m^3) since 31st March 2015 (Entekhabi et al., 2010). The use of SMAP observations for monitoring flash droughts holds promise due to its accuracy, global coverage, and short revisit time (2-3 days). While L-band microwave retrievals by SMAP are limited to the soil surface ($\sim$5 cm), significant information may be inferred from these observations about basin-scale water balance (Koster et al., 2018), evapotranspiration (Purdy et al., 2018), land-surface hydrological fluxes (Sadeghi et al., 2020), irrigation (Lawston et al., 2017), land-atmosphere interaction (McColl et al., 2017), and rootzone soil moisture dynamics (Pablos et al., 2018; Reichle, de Lannoy, et al., 2017) etc. Persistent stress in the surface SM is often indicative of severe SM deficit in the deeper soil profiles due to strong interconnection between the soil layers (except in arid regions where surface and rootzone may hydrologically decouple) through advective and diffusive soil hydrologic processes (Hirschi et al., 2014; Pollacco & Mohanty, 2012; Sehgal et al., 2017; Sehgal & Sridhar, 2019).

In the absence of long-term (climatological length) observations, SMAP observations are used to enhance existing drought monitoring capabilities using hydrological modeling and/or data assimilation. For example, Sadri et al. (2020) combined SM observations from SMAP and SMOS and developed a global drought monitor using a parametric distribution of monthly SM observations. Mladenova et al. (2019) assimilated SMAP observations into the United States Department of Agriculture Foreign Agricultural Service (USDA-FAS) Palmer model to enhance existing global drought monitoring capabilities. Previously, Sadri et al.

(2018) proposed using θ_{RS} to bias-correct SM simulations from the Variable Infiltration Capacity (VIC) model to estimate drought severity across Contiguous U.S (CONUS).

Alternatively, several studies rely on the development of a SM-based index to estimate the (plant) available water content using soil water retention parameters (SWRPs), like field capacity and wilting point (Hunt et al., 2009; Mozny et al., 2012; Sridhar et al., 2008; Bachmair et al., 2018; Martínez-Fernández et al., 2015, 2016). The relative fraction of available water content compared to the maximum (plant) available water (the difference between field capacity or critical point and wilting point) is used as an indicator of drought stress. The SWRPs for these studies are often estimated using either laboratory tests or, are estimated using soil texture (and mineral/carbon composition) information based on pedotransfer functions (PTF). One recent application of θ_{RS} for drought monitoring is provided by Mishra et al. (2017), who developed a soil moisture deficit index using SWRPs from PTFs by Saxton and Rawls (2006). A similar approach is adopted by other studies using SMAP for drought monitoring in several parts of the world (Ajaz et al., 2019; Bai et al., 2018; Liu et al., 2017). Using SWRPs for soil moisture stress estimation does not require long-term SM records or model simulations to estimate SM anomalies, and hence, can be applied across the globe without any explicit dependence on complex models and uncertainty related to model parameter estimation and/or calibration.

While PTFs are a convenient tool to estimate SWRPs using minimal information about soil texture/ composition at point or field-scale, their application at continuous and large spatial scales suffer critical limitations. PTFs are developed using limited measurements made at smaller extents, fine support scale, and/or irregular spacing. The spatial dependencies in the input variables of the PTFs do not translate correctly to the output over large spatial scales with heterogeneous land-surface and soil properties (Chakraborty et al., 2020; Pachepsky & van Genuchten, 2011). Hence, an extrapolation of PTFs beyond respective geographic region of their development may yield erroneous results (Hodnett & Tomasella, 2002; Santra et al., 2018). In addition, global soil databases required for application of these PTFs at regional/ global extent are based on limited soil profiles and coarse resolution soil maps which lack local coverage in several regions of the world (Shangguan et al., 2014). At large spatial scales, multiple biophysical controls like topography, vegetation, hydroclimate, etc. exert dominant control over footprint-scale SM dynamics rather than soil characteristics (Crow et al., 2012; Gaur & Mohanty, 2013, 2016, 2019; Laio et al., 2001). These biophysical controls moderate the transition of RS footprint between energy-limited (no stress) and moisture-limited (stressed) regimes (Akbar et al., 2018; Sehgal et al., 2020), thus governing the response of SM to meteorological anomalies. Hence, the SWRPs used for estimating SM stress for the RS-footprint must capture the "*effective*" footprint-scale SM dynamics

as a result of subgrid-scale soil-atmosphere-plant processes, land-surface heterogeneity, and their temporal variability.

The current methods on flash drought characterization are broadly limited to two categories: i) Stress-based and ii) Change-based approach (Y. Liu et al., 2020). The stress-based method uses standardized matrices like Standardized Evaporative Stress Ratio (SESR) (Christian et al., 2019; Nguyen et al., 2019) to quantify flash droughts. The change-based approach is based on the rate of intensification of drought severity using matrices like SM percentile (Liu et al., 2020; Mahto & Mishra, 2020) or composite drought severity estimates like U.S. drought monitor (L. G. Chen et al., 2019; Otkin et al., 2018). However, a robust operational flash drought monitoring framework must combine the stress-based approach with the change-based assessment to provide early identification of impending flash droughts using the current hydrologic state and the prevailing rate of intensification of hydrologic anomalies in near-real-time.

To address the aforementioned limitations of i) limited θ_{RS} records ii) non-linear controls on θ_{RS} dynamics and the iii) urgent need to combine both change-based and stress-based matrices for characterizing flash drought severity, we propose a new global meteorological drought indicator, Flash Drought Stress Index (FDSI), as a combination of footprint-scale Soil Moisture Stress (SMS, state of moisture deficit) and Relative Rate of Drydown (RRD, rate of intensification of moisture deficit). FDSI follows a non-linear relationship with θ_{RS}, governed by the footprint-scale SM drydown parameters (thresholds of soil hydrologic regimes and the rate of transition from wet- to dry phase). FDSI distinctively identifies flash droughts based on moderate-to-high SMS coupled with moderate-to-high RRD. Dependence on footprint-specific, seasonal drydown parameters yield FDSI sensitivity to the subpixel-scale land-surface heterogeneity and dominant geophysical controls (topography, vegetation, soil etc.) on soil moisture dynamics at SMAP-footprint scale. The advantage of temporally variable, footprint-scale SWRPs over static PTF-based parameters in estimating SMS is examined in the study at a global extent.

We demonstrate the application of the proposed index at a regional/ continental scale for different parts of the world in capturing select drought events. The 2017 flash drought in the American Northern Great Plains (NGPs) is mechanistically evaluated in terms of RRD, SMS and FDSI, to highlight the advantages of the proposed approach in early detection and classification of flash droughts using data and parameters derived from θ_{RS}. The study examines the timescales and strength of relationship between the drivers (meteorology) and response (vegetation health) of variability in FDSI globally to enhance the interpretability of the index for diverse applications.

5

2 Dataset

2.1 Satellite SM data from SMAP

We use global surface SM observations (θ_{RS}) from Soil Moisture Active Passive (SMAP, level 3, version 5) from 31st March 2015 to 19th March 2019 for this study. SMAP uses an L-band microwave radiometer at 1.41 GHz to retrieve global surface (0-5 cm) SM with 2-3 days revisit at the radiometer footprint of ∼40-km) gridded at 36-km (nested) Equal-Area Scalable Earth grid version-2 (Entekhabi et al., 2010; O'Neill, 2018). Quality-flagged data, including pixels with high water fraction (>1%), high radio frequency interference and vegetation water content (VWC), snow cover, flooding, large and highly variable slopes, or urban areas, is omitted from the analysis due to high retrieval uncertainty. We use a custom selective filtering of θ_{RS} based on VWC (≥ 7 kg/m^2) to exclude pixels from deciduous, evergreen and mixed forests (Chan et al., 2013). This prevents conservative filtering of SMAP retrievals over croplands and grasslands, thus, increasing the spatial coverage of θ_{RS} while not drastically compromising the retrieval accuracy (Akbar et al., 2018). We use both descending (6 A.M.) and ascending overpass (6 P.M.) retrievals to benefit from a higher temporal sampling frequency. Both AM/PM retrievals offer accurate measurements within the mission accuracy target of ± 0.04 m^3/m^3 unbiased root mean squared error for unfrozen land surfaces due to improved land surface temperature correction approach implemented in the recent versions of SMAP products (Jackson et al., 2018; O'Neill, 2018). To remove the influence of diurnal variability, quality screened SMAP observations used in the study are linearly interpolated to a uniform daily sampling frequency (6 A.M. local time). Hyper-arid regions (based on classification by UNEP (1997)) like the Arabian peninsula and Sahara desert removed from the analysis due to small dynamic range, high noise and dry-bias in SMAP retrievals (Burgin et al., 2017; Kolassa et al., 2018; Reichle et al., 2015). While newer versions of SMAP level 3 SM are available during the development of this study, we use version 5 for consistency with the global SWRPs developed by Sehgal et al. (2020).

2.2 Footprint-scale soil moisture drydown parameters

Assuming the net lateral fluxes to be negligible for a large SMAP footprint (36-km) of a uniform support depth (∼5cm), the loss in θ_{RS} after precipitation can be attributed to infiltration (I), evapotranspiration (ET), and drainage (D). The functional relationship between $[\theta_{RS}]$ v/s $[-\Delta\theta_{RS}/\Delta t]$ is called SM drydown curve, where $[-\Delta\theta_{RS}/\Delta t]$ is the rate of loss of SM between time t and t-1, and $-\Delta\theta_{RS} = \theta_{RS}{}^t - \theta_{RS}{}^{t-1}$ (negative sign indicates net loss of SM). The SM drydown curve can be approximated as a piecewise-linear curve, where each piece/limb represents a distinct hydrologic regime i.e., i) gravity-drainage (G), ii) energy-limited wet phase (W), iii) moisture-limited transitional phase (T) and iv) dry
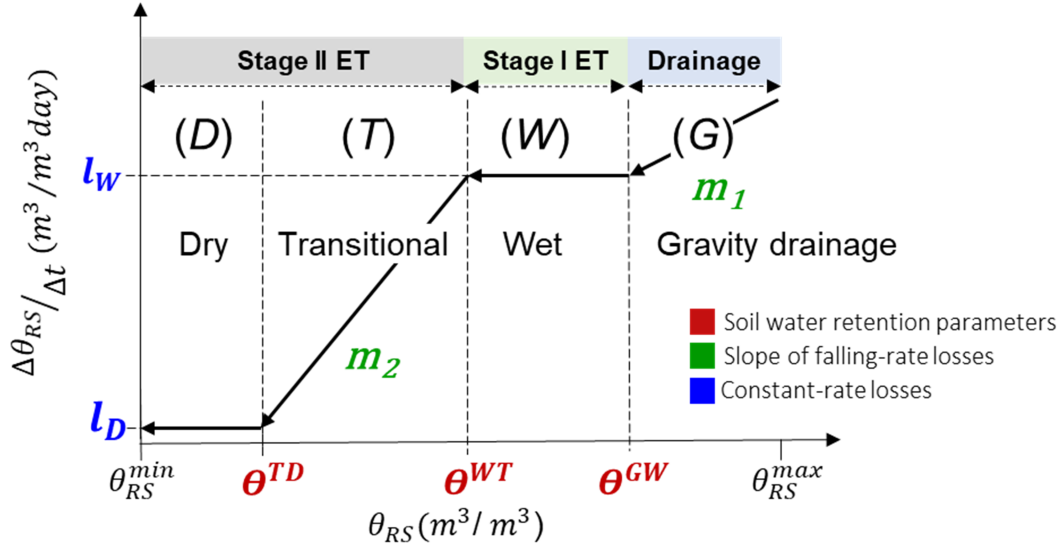
Figure 1. A schematic of soil moisture drydown pathway. Three parameters used in development of FDSI are θ^{WT}, θ^{TD} and m_2.

phase (D) in the order of decreasing θ_{RS}. Depending on the seasonal availability of moisture and energy, several smaller subsets of the complete drydown curve are commonly observed GW, W, WT, WTD, TD, T, D at the RS-footprint scale (Akbar et al., 2018; Sehgal et al., 2020). Mathematically, a SM drydown curve at RS-footprint is governed by a subset of seven parameters comprising of the transition points between consecutive hydrologic regimes (θ^{GW}, θ^{WT}, θ^{TD}), the slope of falling-rate losses — the gravity-drainage and transitional phase (m_1 and m_2 respectively) and the constant-rate loss during wet and dry phase (l_W and l_D). A typical SM drydown curve observed at RS-footprint is shown in Figure 1.

The rate of transitions from energy-limited to the moisture-limited regime is given by m_2 and indicates the land-atmospheric coupling strength for the pixel. The footprint-scale SWRP$_{eff}$ are given by θ^{GW}, θ^{WT}, θ^{TD} which are assumed to be analogous to the field capacity, critical point (SM at the intersection of phase I and phase II ET) and wilting point respectively as defined at the field scale (Laio et al., 2001; Rodriguez-Iturbe et al., 1999; Rodriguez-Iturbe, 2000). Seasonal (December-February, March-May, June-August, September-November) estimates of three parameters, namely, θ^{WT}, θ^{TD} and m_2 from Sehgal et al., 2020 are used in the development of FDSI in this study.

2.3 Meteorological and vegetation drought indices

Two indices, namely Vegetation Health Index (VHI, Kogan (1997, 2002, 2018) and Standardized Precipitation Evapotranspiration Index (SPEI, Vicente-Serrano et al. (2010)

are used for global-scale performance evaluation of FDSI. Use of VHI and SPEI facilitates comparison of FDSI with both the drivers (evapotranspiration and precipitation) and response (vegetation conditions) to drought stress across different spatial and temporal scales.

2.3.1 SPEI

SPEI is a popular multiscale drought index based on precipitation and atmospheric evaporative demand. Calculation of SPEI is based on the estimates of accumulated water deficit/surplus at different time scales based on climatic water balance and adjustment to a log-logistic probability distribution. Due to its multiscale nature (1- to 48-months) and dependence on evapotranspiration and precipitation, SPEI is considered suitable to characterize the hydrological, agricultural, and ecological impacts of droughts (Beguería et al., 2010; Vicente-Serrano et al., 2012). The relationship of SPEI with various hydrological variables, vegetation dynamics and other drought indices is widely studied (Bachmair et al., 2018; Peña-Gallardo et al., 2019; Touma et al., 2015; M. Zhao et al., 2017; Ziese et al., 2014). For this study, we use global monthly SPEI at 1-month accumulation timescale (SPEI-1) as an indicator of transient meteorological drought from April 2015-December 2018 at 0.5°(50-km) spatial resolution (SPEIbase-version 2.6, Beguería and Vicente Serrano (2020)).

2.3.2 VHI

Estimation of VHI is based on a combination of the Normalized Difference Vegetation Index (NDVI) and brightness temperature (TB, 10.3-11.3-µm infrared) (Gitelson et al., 1998; Kogan, 2002) to provide a balanced estimation of vegetative stress due to increased land-surface temperature and decreasing SM. VHI assumes a decrease in the vegetation cover with to an increase in land-surface temperature and depleting SM leading to reduced evapotranspiration (Karnieli et al., 2006; Lambin & Ehrlich, 1996). Application of VHI has been demonstrated for the assessment of crop yield/loss (Kogan et al., 2012; Kogan, 2018), agricultural drought (Bachmair et al., 2018; Bhuiyan et al., 2017; Wu et al., 2020), impacts of irrigation practices (Ambika & Mishra, 2019; Sahoo et al., 2020), impacts of oil spill on vegetation (Hester et al., 2016), etc. This study uses VHI based on multispectral observations from the Advanced Very High-Resolution Radiometer (AVHRR) satellite. The dataset is provided by NOAA's Center for Satellite Applications and Research (STAR), as a 7-day composite at a global scale at 4-km spatial resolution, which is aggregated to SMAP footprint scale (36-km) using bilinear aggregation. VHI is expressed in percentages, with values <40% indicating severe drought stress (Kogan, 2002, 2018, 1997) and VHI >60% indicates high vegetation productivity. As SMAP retrieval algorithm (O'Neill, 2018)

uses Normalized Difference Vegetation Index (NDVI) climatology from Moderate Resolution
Imaging Spectroradiometer (MODIS), use of vegetation index from AVHRR helps prevent
spurious error correlation of VHI with SMAP-based indices.

3 Methodology

3.1 Drought assessment matrices

The formulation of FDSI is based on two matrices, namely Soil moisture Stress (SMS)
and Relative Rate of Drydown (RRD), to capture the severity and the rate of intensification
of droughts, respectively. The matrices are defined as follows:

3.1.1 Soil Moisture Stress (SMS)

SMS is defined as a unitless metric which maps the transition of the soil hydrologic
regime of a SMAP footprint from energy-limited ($\theta_{RS} > \theta^{WT}$, no stress) to dry conditions
($\theta_{RS} < \theta^{TD}$, high stress) moderated by an exponent n (Eq. 1). For any time, t, the value
of $\boldsymbol{f}(\theta_{RS}, \text{SMS})$ is given by a non-linear, S-shaped relationship as below:

$$SMS_t = \frac{1}{1 + \left(\frac{\theta_{RS,t}}{\theta_{IP}}\right)^n} \tag{1}$$

where

$$\theta_{IP} = \left(\frac{\theta^{TD} + \theta^{WT}}{2}\right) \tag{2}$$

and

$$n = \lambda \;.\sqrt{m_2} \tag{3}$$

The value of SMS approaches zero [-] and unity [-] asymptotically as the value of fraction
θ_{RS}/θ_{IP} increases or decreases respectively, moderated by the exponent n. The inflection
in $\boldsymbol{f}(\theta_{RS}, \text{SMS})$ occurs at $\theta_{RS} = \theta_{IP}$, which yields SMS= 0.5 [-] as shown in Figure 2a. The
parameter θ_{IP}, called the inflection point, is defined as the average of θ^{TD} and θ^{WT} (in
m^3/m^3, Eq. 2). High (or low) θ_{IP} value leads to the transition of a pixel into stressed
conditions at relatively higher (or lower) θ_{RS}. The exponent n used in the formulation of
SMS, called the shape parameter, governs the steepness of $\boldsymbol{f}(\theta_{RS}, \text{SMS})$, moderating the
sensitivity of SMS (higher n leads to higher sensitivity).

The shape factor, n, used in $\boldsymbol{f}(\theta_{RS}, \text{SMS})$ is conditioned upon the land-atmospheric
coupling strength of the SMAP footprint (Eq. 3), which is given by the slope of the transi-
tional phase in a typical SM drydown curve and is given by the parameter m_2 (Figure 2a).
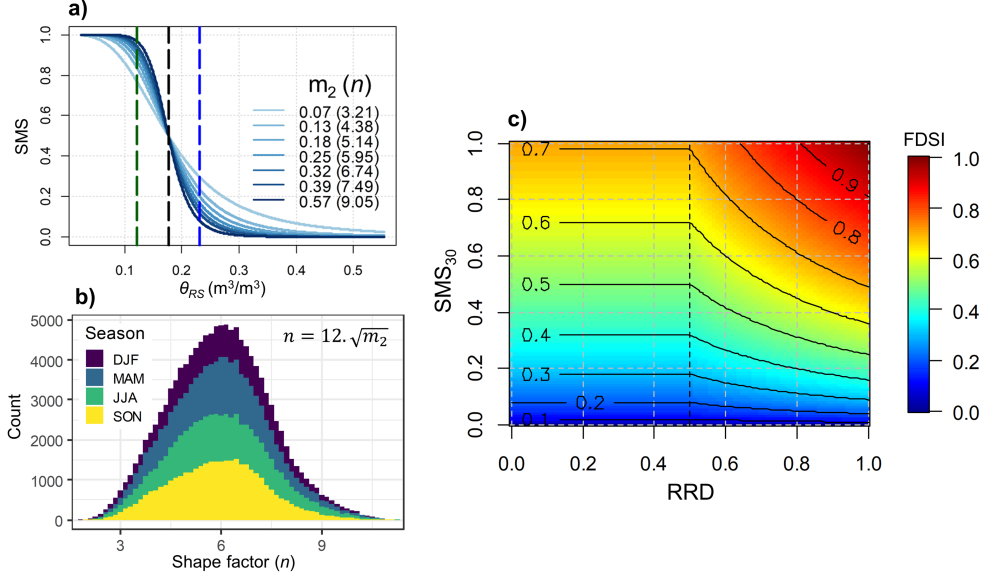SMS for the pixels with a high value of m_2 have a relatively high value of n, and hence, a

Figure 2. *a*) A sample plot for $\boldsymbol{f}(\theta_{RS}, \text{SMS})$ with different values of n (given in parenthesis) using seasonal average values of θ^{WT} and θ^{TD} for a pixel in College Station, Texas, US (30.63°N, 96.33°W). The selected values of m_2 for the schematic correspond to the 2.5, 15, 30, 50, 70, 85, 97.5^{th} percentile of global m_2 estimates (all seasons combined) and the seasonal average values of θ^{WT} and θ^{TD} for the sample pixel 0.23 m³/m³ and 0.12 m³/m³ respectively (θ_{IP}=0.175 m³/m³). Observe that the steepness (sensitivity) of the $\boldsymbol{f}(\theta_{RS}, \text{SMS})$ curve increases with the increasing value of n for a fixed value of θ_{IP}. *b*) Stacked histogram of shape factor values for the four seasons (DJF, MAM, JJA, SON) from the global estimates of m_2. *c*) A contour plot of the trivariate relationship between θ_{RS} (x-axis), SMS₃0 (y-axis) and FDSI (z-axis and contours). Flash drought is characterized with FDSI ≥ 0.71 (shown in darker shades of red in the top-right quadrant).

heightened sensitivity to transient atmospheric conditions and vice-versa for a given value of a multiplier λ. The value of λ is taken to be 12 to attain the median global values of n = 6 following Cammalleri et al. (2016). The global values of m_2 are observed to be (right) skewed, however, the square root transformation (i.e. $\sqrt{m_2}$) is used to attain a near-normal distribution for n (Figure 2b). The 99% confidence band for n = [2,10]. To illustrate the influence of variability in m_2 (and hence, n) on the estimates of SMS, a plot of $\boldsymbol{f}(\theta_{RS}, \text{SMS})$ using seasonal average values of θ^{TD} and θ^{WT} is shown in Figure 2b for a sample pixel.

Seasonal estimates of SWRP_{eff} for all four seasons may not be available for some pixels due to i) long-term missed retrievals in high-latitude regions due to persistent snow cover, or ii) dominance of partial drydown pathway i.e. {W} (wet), {D} (dry), {G} (gravity drainage), {GW} (gravity drainage and wet). The missing values of the SWRP_{eff} for any season are gap-filled using the average values of the available seasonal SWRPs for estimating θ_{IP}. In the case of the pixels following the drydown pathway {T} (transitional) and {TD} (transitional and dry), the value of θ^{WT} is assumed to be the 1.05 times the maximum

10

seasonal value of SM for the pixel. The multiplier 1.05 is selected out of several other values (0.15, 1.5 and seasonal maximum) based on marginal performance improvement in correlation of the proposed index w.r.t SPEI-1 (not shown here for brevity). A spatiotemporally varying field of the global θ_{IP} and n is generated for each calendar day using the seasonal estimates of θ^{TD}, θ^{WT} and m_2. A moving-average filter of a length of 30-days (centered at $t=0$) is carried out on the temporal values of the parameters for each pixel to facilitate a seamless transition of the SMS between the seasons.

3.1.2 Relative Rate of Drydown (RRD)

RRD [-] is an indicator of the rate of intensification of SM stress based on the prevailing Rate of Drydown (RD) of θ_{RS} in the last 30 days vis-à-vis the seasonal values of m_2. Similar to SMS, RRD follows a non-linear formulation given as:

$$RRD_t = \frac{1}{1 + \left(\frac{m_2}{RD_t}\right)^6} \tag{4}$$

where RD_t is the slope of the linear fit to $[\theta_{RS}]$ v/s $[-\Delta\theta_{RS}/\Delta t]$ observations during the transitional phase ($\theta^{TD} < \theta_{RS} < \theta^{WT}$) of SM drydown using observations in the interval t to t-30, where t=time in days. The value of RRD_t approaches zero [-] and unity [-] asymptotically as the fraction m_2/RD_t increases or decreases respectively with a central value of 0.5 when $RD_t = m_2$. The value of the non-linear exponent is fixed to be 6, consistent with the median value of n used for SMS. In the event of low data availability (less than 10 observations) or curve fitting accuracy ($R^2 < 0.2$), RRD is assumed to be 0.5.

3.1.3 Flash Drought Stress Index (FDSI)

As per a widely accepted definition (Pendergrass et al., 2020), flash drought episodes develop within a period of 1-month with hydrologic deficits developing within a 2-week period and sustaining for another 2 weeks. Consistent with that definition, FDSI is based on a combination of a 30-day retrospective moving average SMS (termed, SMS_{30} as shown in Eq. 5) and RRD as follows:

$$SMS_{30,t} = \left(\sum_{i=t}^{t-29} SMS_i\right)/30 \tag{5}$$

$$FDSI_t = \begin{cases} \sqrt{SMS_{30,t} \times RRD_t} & if\, RRD_t > 0.5 \\ \sqrt{SMS_{30,t} \times 0.5} & if\, RRD_t \le 0.5 \end{cases} \tag{6}$$

11

Eq. 6 provides a unique relationship between FDSI with changes in SMS_{30} and RRD as shown in Figure 2c. When RRD $\leq$ 0.5, FDSI is proportional to $\sqrt{SMS_{30}}$ with theoretical maximum of 0.707 when the maximum value of SMS_{30} equals 1. The values of FDSI >0.71 is achieved only during above normal drydown rates (i.e. when RRD >0.5). Use of the square root transformation in Eq. 6 preserves the density distribution of FDSI consistent with SMS_{30} and RRD. Due to its reliance on θ_{RS}, FDSI can be interpreted as a meteorological drought indicator. However, flash droughts can be differentiated from other meteorological anomalies based on different FDSI thresholds. Flash droughts are identified with values of FDSI $\geq$ 0.71, while FDSI >0.5 is considered as the threshold for abnormally dry conditions for the purpose of this study.

Previously, several studies have followed the seminal works of (van Genuchten, 1987; van Genuchten & Gupta, 1993) to develop non-linear, S-shaped relationships for diverse applications in soil hydrology like modeling root water uptake—soil water potential (Skaggs et al., 2006), relative crop yield—soil salinity (Skaggs et al., 2014; van Straten et al., 2019) etc. Studies have also demonstrated the application of S-shaped curves to model SM—soil stress relationship (Ajaz et al., 2019; Cammalleri et al., 2016). However, previous studies rely on using soil textural class information in deriving the estimated value of θ_{IP} while using a fixed value of n (depending on the application, soil type and vegetation), thus making the relationship purely dependent on the soil type for a given value of n. However in this study, the parameters θ_{IP} and n for SMS and m_2 for RRD are obtained using the seasonally derived parameters of the footprint-scale drydown curves of θ_{RS}. Hence, FDSI is sensitive to temporally varying subpixel-scale land-surface heterogeneity due to vegetation and SM distribution; and the soil-vegetation-atmospheric controls which moderate the SM dynamics at RS-footprint scale.

3.2 Pedotransfer function-based estimates of SM stress

To provide a comparison with the proposed approach for calculating SMS, we use the PTFs from Saxton and Rawls (2006) to estimate SWRPs using soil textural properties and a time invariant value of n=6 to derive SMS_{PTF}. Soil textural information on sand, clay and organic matter content is obtained from the Harmonized World Soil Database (version 1.2) (Nachtergaele et al., 2012). Organic matter is obtained from the organic content using a factor of 0.58 as proposed by (Pribyl, 2010). Saxton and Rawls (2006) PTF is selected based on its extensive use in the field of hydrology for estimation of SWRPs at large spatial scales (Martínez-Fernández et al., 2015; Mishra et al., 2017) and its ability to estimate both wilting point and field capacity. Based on the traditional definition, the wilting point of soil is defined as the volumetric SM at 1500 kPa pressure, given by $\theta_{(\psi=1500kPa)}$. Similarly,

332 $\theta_{(\psi=33kPa)}$ represents the field capacity of soil, defined as the volumetric SM at 33 kPa

333 pressure. The critical point is assumed to be half of the field capacity following (Cammalleri

334 et al., 2016). Accordingly, the formulation of SMS_{PTF} uses a modification of Eq. 1 as

335 $\theta_{IP} = \frac{\theta_{(\psi=1500kPa)} + \theta_{(\psi=33kPa)}/2}{2}$.

3.3 Time-lagged Anomaly Correlation

337 We use Anomaly Correlation (AC) to quantify the linear relationship (strength and

338 timescale) of FDSI with meteorological controls (SPEI-1) and the response of vegetation

339 health (VHI) to FDSI. The formulation of AC follows that of Pearson's correlation coeffi-

340 cient; except, the coefficient is computed using temporal anomalies of the dataset. AC is

341 popularly used to quantify predictive skill score of the climate model outputs (Dong et al.,

342 2019; T. Zhao et al., 2019, 2017).

343 Time-lagged AC for a control/trigger variable (X) and a time-lagged (by time l) re-

344 sponse variable (Y) at a temporal scale, s, is computed (significance level of 0.05) as below:

$$AC_l = \frac{\sum_t \left[\left(X_{s,t} - \overline{X_s}\right) - \overline{\left(X_{s,t} - \overline{X_s}\right)} \right] \times \left[\left(Y_{s+l,t+l} - \overline{Y_{s+l}}\right) - \overline{\left(Y_{s+l,t+l} - \overline{Y_{s+l}}\right)} \right]}{\sqrt{\sum_t \left[\left(X_{s,t} - \overline{X_s}\right) - \overline{\left(X_{s,t} - \overline{X_s}\right)} \right]^2 \sum_t \left[\left(Y_{s+l,t+l} - \overline{Y_{s+l}}\right) - \overline{\left(Y_{s+l,t+l} - \overline{Y_{s+l}}\right)} \right]^2}} \tag{7}$$

$$AC = \max_l |AC_l| \tag{8}$$

346 where, $X_{s,t}$ are the observations of the control variable, X, recorded at time t, at a temporal

347 scale, s (month/ week). The value of Y observed at a lag, l, with respect to $X_{s,t}$ is given

348 by $Y_{s+l,t+l}$. $\bar{X}_s$ and $\bar{Y}_s$ are the climatological mean of X and Y for each s for the period

349 of analysis. For VHI and SPEI-1, s corresponds to weekly (s=1 to 52) and monthly (s=1

350 to 12) timescale respectively. At large spatial scales, meteorology is the primary driver of

351 the temporal SM dynamics, while, SM availability is a strong predictor of vegetation health

352 and productivity. Hence, AC_l is calculated between monthly SPEI-1 and time-lagged (up

353 to three months) mean monthly FDSI (s=1 to 12, l=0 to 3). AC_l between mean weekly

354 FDSI and time-lagged (up to 10 weeks) 7-day composite VHI provides the skill of FDSI

355 in forecasting vegetation health (s=1 to 52, l=0 to 10). The maximum lag times in the

356 response variables is selected to capture the sub-seasonal to seasonal variabilities in the

357 dataset (up to 3 months/ 10 weeks). For each pixel, maximum (absolute) AC_l (Eq. 8) and

358 the corresponding time-lag, l, is recorded.

359 AC provides a more rigorous assessment of the relationship between two variables than

360 Pearson's correlation by excluding the influence of seasonal and sub-seasonal variabilities in

361 the observations (Reichle, Draper, et al., 2017). Use of AC is particularly suited in this study

as use of seasonal drydown parameters in the formulation of FDSI may lead to potential sub-seasonal periodicities in the dataset leading to spuriously high correlation with SPEI-1 and VHI.

4 Results and discussion

4.1 Characteristics of FDSI parameters

4.1.1 Spatial and temporal variability in SMAP-based θ_{IP} and n

A global season-wise comparison of θ_{IP} and n, is shown in Figure 3 to help understand the characteristic properties of $\boldsymbol{f}(\theta_{RS}, \text{SMS})$ and $\boldsymbol{f}(\text{RD}, \text{RRD})$ across different hydroclimates, landuse/landcover and/or soil types. The parameters, θ_{IP} and n, show a significant spatiotemporal variability in response to the changing subgrid-scale heterogeneity (vegetation and SM distribution), and availability of moisture and energy for the SMAP footprint. Climate has a dominant influence on the effective SM dynamics at SMAP footprint. The values of θ^{WT} are observed to be higher (hence, higher θ_{IP}) for subhumid and humid climates compared to the arid and semi-arid regions. In regions with semi-arid or arid climate, pixels with high clay content (>40% w/w) show a greater value of θ^{TD} (and hence, θ_{IP}). The temporal variability in θ_{IP} is observed to be higher for pixels with clayey soils, irrespective of the climate, due to susceptibility to shrinking and swelling (Boivin, 2011; Boivin & Garnier, 2004). Such condition is observed in (not limited to) Eastern Texas, Central India, and Pampas of South America. The value of θ^{TD} increases in clayey soils during dry seasons and cause an increase in θ_{IP} as seen in Figure 3.

In moisture-limited conditions, SM exerts the limiting control on the variance in evapotranspiration in response to the atmospheric moisture (Dirmeyer, 2011). The terrestrial component of the land-atmospheric coupling strength is measured by the parameter m_2, and is governed by potential evapotranspiration (PET). Typically, arid and semi-arid regions show higher values of n due to stronger land-atmospheric coupling compared to humid and sub-humid regions (Figure 3). The influence of high PET is reflected in higher values of n in the southern hemisphere during boreal winter for Southern America, Southern Africa, and large parts of Australia. During MAM and JJA, large parts of the northern hemisphere including Central Asia, U.S. South West, Sahel region of Africa and Indus Valley, show higher values of n. The spatiotemporal dynamics of land-atmospheric coupling directly impacts the sensitivity of $\boldsymbol{f}(\theta_{RS}, \text{SMS})$ to the variability in θ_{RS} through the parameter n. Hence, higher PET leads to higher land-atmospheric coupling and higher sensitivity of $\boldsymbol{f}(\theta_{RS}, \text{SMS})$, and vice-versa. In humid and subhumid climates, strong vegetation-atmospheric coupling (especially in croplands, forests and savannah grasslands during the growing season) can help
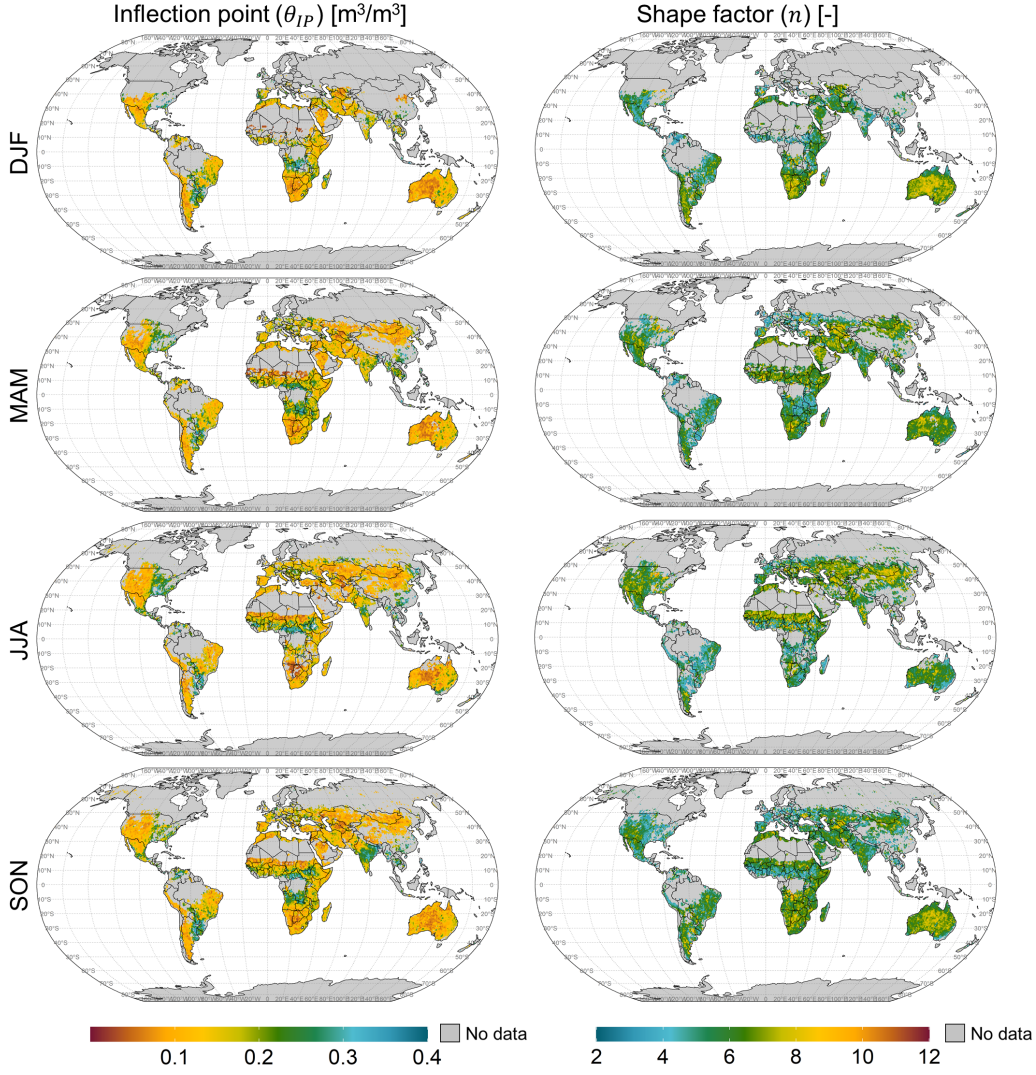
14

Figure 3. (**Left**) Season-wise spatial plots of the inflection point (θ_{IP} in m^3/m^3) using SMAP-based seasonal estimates of θ^{WT} and θ^{TD} (**Right**) Season-wise SMAP-based estimates of the shape factor (n, unitless). Gray area in the spatial plots indicate pixels with masked/ flagged data.

reduce the sensitivity of $\boldsymbol{f}(\theta_{RS}, \mathrm{SMS})$ by slowing down the rate of drydown (and hence, the value of m_2). Access to upward movement of water in humid climates due to matric suction with shallow ground table and high transpiration leads to strong vegetation-atmospheric coupling (Zscheischler et al., 2015). As a results, the value of m_2 decreases, reducing the sensitivity of $\boldsymbol{f}(\theta_{RS}, \mathrm{SMS})$ for humid and subhumid ecosystems.

4.1.2 Comparison of θ_{IP} from PTF and SMAP

Figure 4a shows the spatial distribution of θ_{IP} based on the PTF. In the absence of vegetation and subgrid-heterogeneity in SM in arid and semi-arid climate regions, soil

15

texture exerts dominant control on the spatial variability of θ_{IP} (Gaur & Mohanty, 2013, 2016). Hence, the estimates of θ_{IP} from SMAP and PTF are observed to be similar in arid and semi-arid climates (Figure 4b). In contrast, significant differences between SMAP- and PTF-based estimates are observed in sub-humid and humid hydroclimates, where climatic and vegetative factors strongly influence the dynamics of SM at the RS-footprint scale (Figure 4b). In humid and sub-humid climates, the median PTF-based estimates of θ_{IP} are observed to be significantly lower compared to SMAP-based estimates by 0.06 m^3/m^3.

Figure 4. **a**) Spatial plots of the inflection point (θ_{IP}, in m^3/m^3) using estimates of $\theta_{(\psi=1500kPa)}$ and $\theta_{(\psi=33kPa)}$ from PTF. **b**) Hydroclimate-wise distribution of θ_{IP} from SMAP and PTF. Grey area in the spatial plots indicate pixels with masked/ flagged data.

Figure 5 provides a comparison between SMS estimated using parameters from SMAP and PTF (referred to as SMS$_{SMAP}$ and SMS$_{PTF}$ here respectively) for three sample locations in different hydroclimates. As shown in Figure 5, the temporal variability in both θ_{IP} and n yields a distinct influence on the characteristics of $\boldsymbol{f}(\theta_{RS}, \text{SMS})$ for each season based on the hydroclimate. Due to the higher value of θ_{IP}, the observed values of θ_{RS} are mapped to a higher value of stress in boreal winter (DJF) and spring (MAM) compared to summer (JJA) and fall (SON) seasons in humid and sub-humid climates. The seasonal variability is compounded for the pixel in Texas (sub-humid climate) with clayey soil as shrinkage and swelling of soil leads to larger inter-seasonal variations in θ_{IP}. Furthermore, humid and sub-humid climates show higher variability in n over the seasons compared to arid and semi-arid regions, thus moderating the steepness of $\boldsymbol{f}(\theta_{RS}, \text{SMS})$ (between 3.32 to 5.15 [-], 4.07 to 5.89 [-] and 4.39 to 5.08 [-] for humid, sub-humid and semi-arid pixel respectively). In contrast, SMS$_{PTF}$ uses time-invariant parameters and is insensitive to the changing subgrid conditions and the soil-vegetation and climate dynamics. This leads to overestimation of SM stress by SMS$_{PTF}$ in arid and semi-arid climates and underestimation of SM stress in humid and sub-humid regions compared to SMS$_{SMAP}$. At a regional/
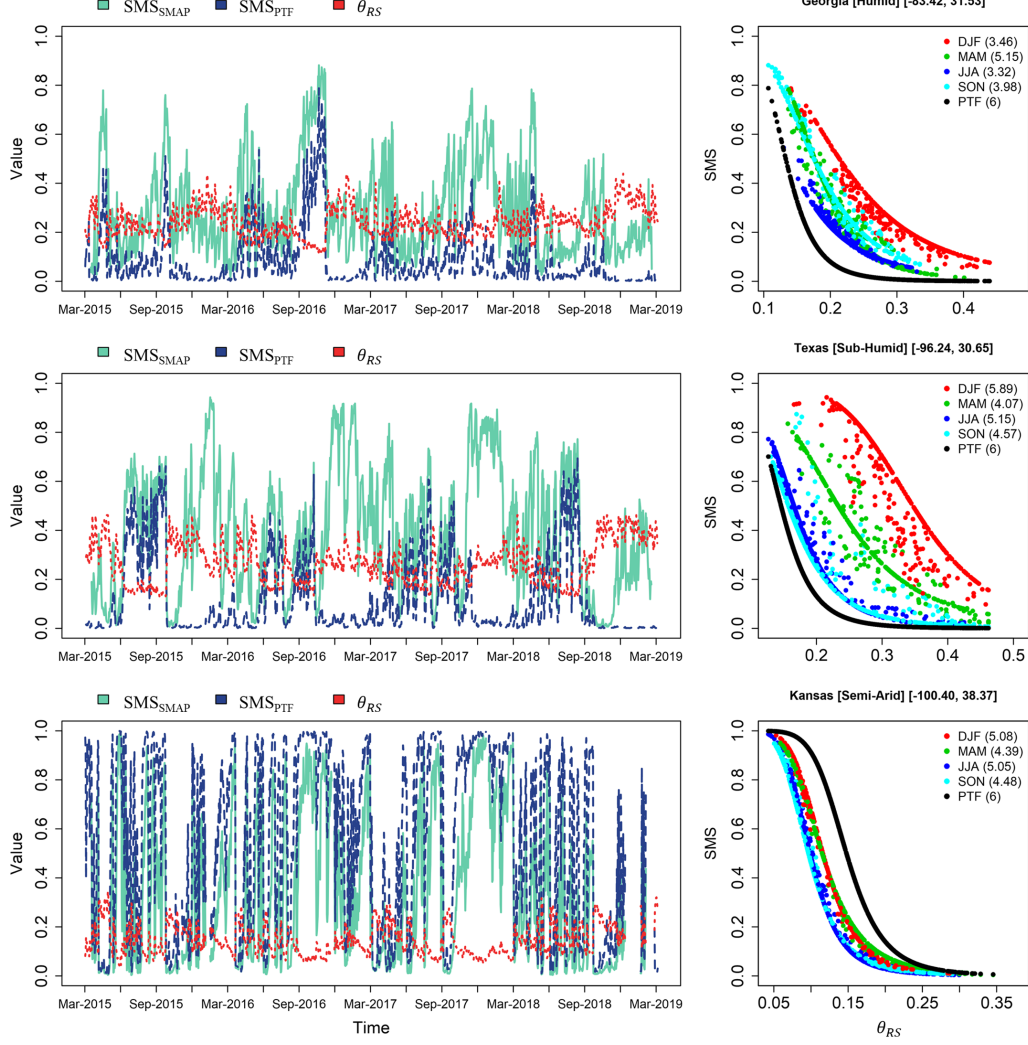
16

Figure 5. *Left*) Time series of θ_{RS}, SMS_{SMAP} and SMS_{PTF} for the three sample locations. *Right*) Plots for $f(\theta_{RS}, \mathrm{SMS})$ using parameters from SMAP and PTF for three sample pixels located in East-Texas (Sub-humid), Georgia (Humid) and Kansas (Semi-arid). The values in the parenthesis show respective values of n for each season/method.

continental scale, insensitivity to changing subpixel properties and large-scale SM dynamics reduces the accuracy of drought severity estimates using SMS_{PTF}. To highlight this issue a CONUS-wide comparison of SMS_{SMAP} and SMS_{PTF} is provided with the drought severity assessment from the U.S. drought monitor at a weekly scale in Section S1 of the supplementary material. Based on the analysis shown in Section S1, and Figure 5, we use SMS, RRD and FDSI based only on the footprint-scale drydown parameters from SMAP (θ_{IP} and m_2) in the subsequent sections of this study.

17

4.2 Performance assessment of FDSI: Comparison with SPEI-1

A global-scale assessment shows high (negative, as low SPEI indicate higher drought stress and vice-versa) AC values between SPEI-1 and FDSI (Figure 6a). Depending on the hydroclimate, θ_{RS} displays short-term memory ranging from several days to multiple weeks (McColl et al., 2017) and is sensitive to transient climatic/ meteorological variability through evapotranspirative, drainage losses, and gain due to precipitation. Strong relationship between SPEI-1 and FDSI is observed for most part of the globe. The median values of AC between SPEI-1 and FDSI is observed to be -0.45 [-] for arid climate and -0.50 to -0.52 [-] for semi-arid, sub-humid and humid regions, with maximum values ranging from -0.76 to -0.87 [-]. Surface SM is known to underestimate temporal hydrometeorological variability under extreme and/or sustained dry conditions as the surface soil profile hydrologically decouples from the rootzone (Hirschi et al., 2014). This explains relatively weaker linear relationship between SPEI-1 and FDSI for arid regions compared to other climates.
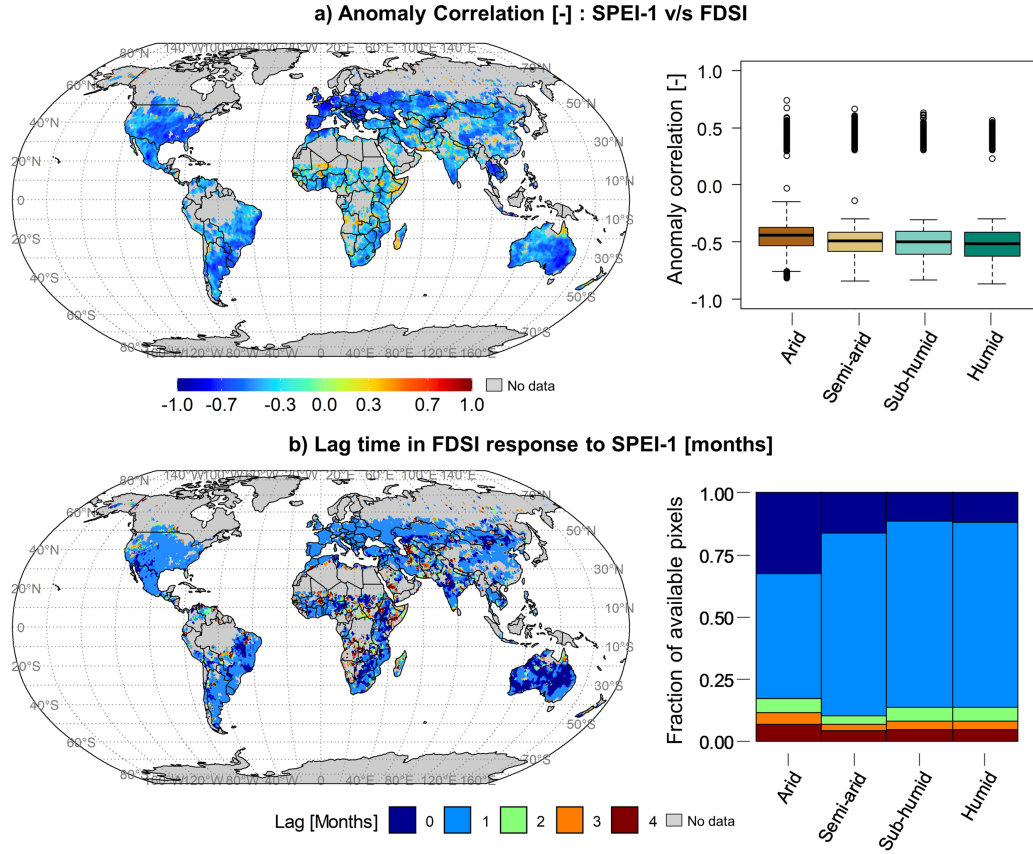
a) Anomaly Correlation [-] : SPEI-1 v/s FDSI

b) Lag time in FDSI response to SPEI-1 [months]

Figure 6. Global maps and sumary of **a**) Anomaly correlation [-] and **b**) Lag time (in months) in FDSI response to monthly SPEI-1. Monthly SPEI-1 and mean-monthly FDSI values are used for the analysis. Anomaly correlation values with p-value >0.05 are excluded from the analysis. Grey area in the spatial plots indicate pixels with masked/ flagged data.

18

As θ_{RS} responds to short-term meteorological variabilities, FDSI anomalies correlates best with the concurrent (0-1 month) SPEI-1 for large parts (19.5 and 66.5% respectively) of the globe (Figure 6b). Higher fraction ($\sim 1/3^{rd}$) of pixels in arid climate show maximum correlation between FDSI and SPEI-1 for the same month ($l=0$) due to stronger land-atmospheric interactions (higher m_2, hence sensitive FDSI) in these regions. Such conditions are observed for regions like Southwestern U.S., large parts of Australia, Western India, Gobi Desert in Mongolia, Kalahari Desert in Southern Africa, among others. For other hydroclimates, a large majority of pixels (over 74% each) displayed 1-month lag in FDSI for maximum (negative) AC with SPEI-1.

A short response time of FDSI to SPEI-1 (0-1 month) supports the applicability of the proposed approach in characterization of global flash droughts. Due to the limitation of the temporal resolution (monthly) of SEPI-1 dataset, sub-monthly dependencies between SPEI-1 and FDSI is not evaluated in this study. However, application of changes in SPEI-1 at a monthly timescale is satisfactorily demonstrated in identifying flash droughts using SPEI-1 (Noguera et al., 2020). Hence the assessment is restricted to using freely available global SPEI-1 dataset at a monthly time-step.
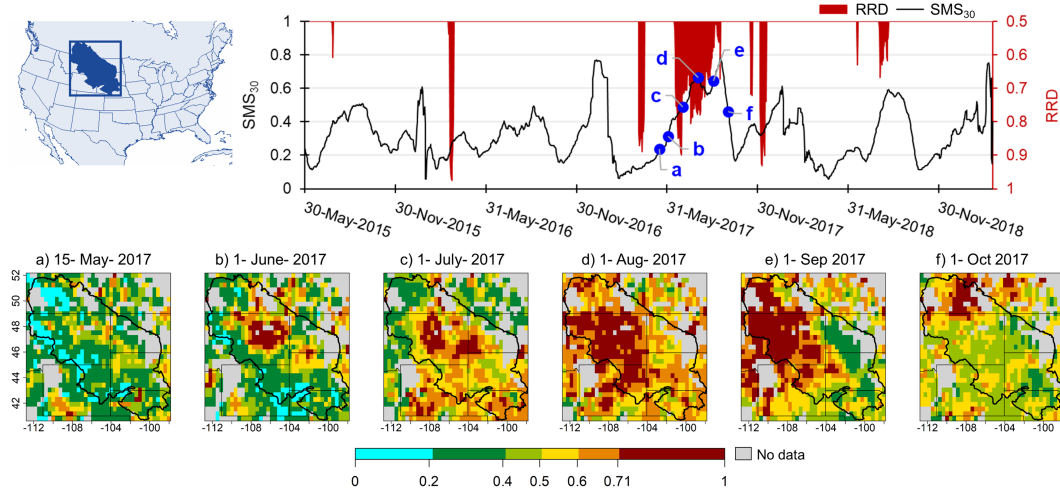

Figure 7. *Top*) Time series of median value of SMS_{30} [-] and RRD [-] for the Northern Great Plains (inset). The blue markers indicate the timeline of FDSI snapshots shown in the panel below. *Bottom*) Snapshots of FDSI [-] over the region during May through October 2017 showing evolution of flash drought over the region. Gray area in the spatial plots indicate pixels with masked/ flagged data.

4.3 Application of FDSI for global (flash) drought monitoring and impact assessment

4.3.1 Mechanistic evaluation of the 2017 Northern Great Plains flash drought

The Northern Great Plains (NGP, western Montana, Wyoming, North- and South-Dakota and parts of Canadian Prairies) experienced an unprecedented flash drought in mid-2017. A mechanistic assessment of the 2017 drought event in the NGP is shown in Figure 7 using FDSI, and its constituent matrices, RRD and SMS_{30}. Large parts of the region are observed to be under normal conditions (FDSI <0.4) till mid-May; however, above-normal temperature and windy conditions caused an increase in the (median) RRD for the region. With the dry conditions prevailing in the subsequent weeks, the SMS_{30} is observed to increase causing an onset of flash drought (FDSI $\geq$ 0.71) in Eastern Montana by the end of May 2017. As SMS_{30} remains high in the subsequent weeks, coupled with high RRD, drought conditions are observed to spread in most parts of the NGP, expanding to the Canadian Prairies. The characteristics of the 2017 episode of flash drought — concurrent high SMS_{30} and RRD for several consecutive weeks, are uniquely distinguishable from the SMS_{30} and RRD relationship from other years in the study period. These observations are consistent with various hydroclimatological studies which identify increased evapotranspiration and rapid loss of SM as the trigger of the 2017 flash drought caused by a combination of record-low precipitation (since 1895) in May-July 2017, above-normal temperatures and high winds from mid-May to June (Mo & Plettenmaier, 2020; Osman et al., 2020; Pendergrass et al., 2020).

4.3.2 Global hotspots of flash droughts

Figure 8a-c provide a spatial distribution of the total number of days under flash drought regime under three FDSI categories (FDSI $\geq$ 0.71, FDSI $\geq$ 0.81 and FDSI $\geq$ 0.91) for longer than 30 days. Several global hotspots of flash droughts are observed, predominantly, in global drylands — Western US, Sahel, large parts of India, Northeastern Brazil, and Central Asia due to strong land-atmospheric interactions and high atmospheric moisture demand in these regions. Large parts of Australia and southern Africa sustained persistent droughts during the study period with intermittent recovery. High FDSI ($\geq$0.91) was seen for Australia and southern Africa due to high SMS_{30}, coupled with high RRD after (any) intermittent precipitation under large vapor pressure deficit and temperature. Figure 8d summarizes the total area (in million km^2) and duration (days) of flash droughts under different severity categories of FDSI. A large area of about 7.8 million km^2 (5.2% of global landmass) is estimated to be impacted by flash droughts lasting from 30-50 days with FDSI
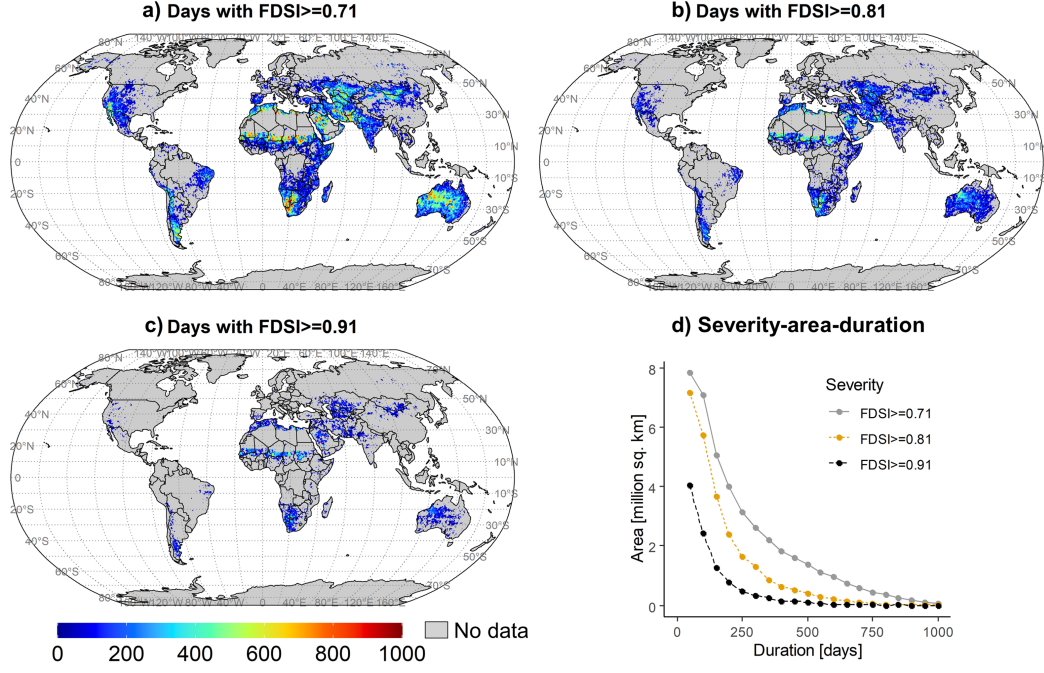
Figure 8. Number of days (from 31st March 2015 to 19th March 2019) under various flash drought stress category **a**) FDSI $\geq$ 0.71, **b**) FDSI $\geq$ 0.81, and **c**) FDSI $\geq$ 0.91 **d**) Estimate of global area (in million km^2) under different flash drought categories. Severity-area estimates exclude masked SMAP pixels. Drought events are identified as at least 30 consecutive days with FDSI $\geq$ 0.71. Gray area in the spatial plots indicate pixels with masked/ flagged data.

$\geq$ 0.71 and with 7.2 million km^2 and 4 million km^2 area under severity of FDSI $\geq$ 0.81 and FDSI $\geq$ 0.91 respectively.

The global hotspots of flash droughts observed in this study closely resemble flash drought occurrence patterns reported by Christian et al. (2020) using global SESR from long-term (1980-2015) reanalysis dataset. However, it is important to note that flash drought hotspots may be more widespread than reported by this study due to the exclusion of flagged/masked SMAP observations (for all seasons) in regions with permanent dense vegetation, snow cover, complex topography etc. (in Alaska, Siberia Northern Europe and Americas and forested regions in Amazon, Eastern U.S., and Central Africa).

A snapshot of select drought events during 2015-2019 (Figure 9) demonstrates the ability of FDSI in capturing emerging and sustained drought events. Figure 9 show regional FDSI conditions during drought intensification in Western US (2016) and Australia (2018), sustained drought conditions in northeastern Brazil (2015) and Southern Africa (2018-19) and drought recovery in India in 2017 after the onset of monsoon.
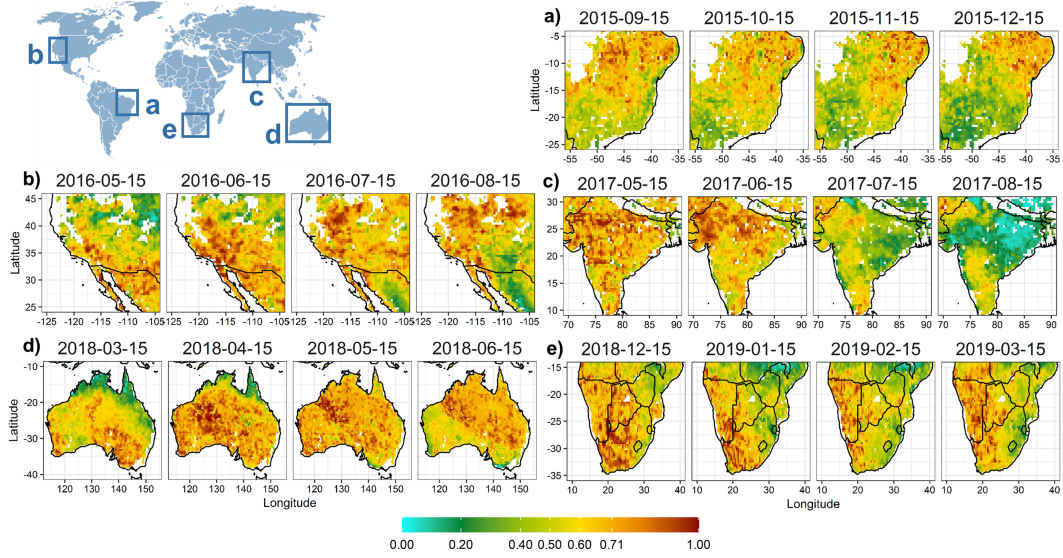
Figure 9. Snapshot of FDSI [-] for some of the prominent droughts during 2015-2019 (in chronological order) **a**) Sustained drought conditions in Northeastern Brazil during September-December 2015, **b**) sustained drought in the Western U.S. during 2016 **c**) Drought recovery with advancing monsoon in the Indian peninsula from May-August 2017 **d**) Intensification of drought severity in Australia from March- June 2018 and **e**) Sustained dry conditions in Southern Africa from December 2018-March 2019.

4.3.3 Predicting global vegetation health using FDSI

A global assessment of the predictive skill for VHI by time-lagged (0 to 12 weeks) FDSI shows a strong linear relationship between FDSI and VHI for large parts of the world (Figure 10). The exact nature of FDSI-VHI relationship is governed by the coupled soil-atmosphere-plant processes and the spatiotemporal variability in vegetation and climate. For the grassland and savannah ecosystems in arid and semi-arid climates, plants display intense competition for moisture and are more sensitive to short-term deficits in the SM (Grossiord et al., 2017; James et al., 2003; Western et al., 2003). Hence, FDSI shows high predictability of VHI in shrublands and grasslands/ savannah ecosystems with a lag of 0-1 week (area-average median AC of -0.49 [-] with a maximum of -0.92 and -0.93 [-] respectively). For mixed forests in sub-humid and humid climates, the response of short-term meteorological variability on vegetation is comparatively low (median AC of -0.37 [-] with maximum value of -0.78 [-]) due to access to SM in the deeper rootzone profile (Z. Chen et al., 2020; Q. Zhang et al., 2017; X. Zhang et al., 2016). Hence, regions like eastern U.S., northern Europe, central Africa, and southern South America show a longer response time to changes in FDSI with 52.5% pixels in mixed forests show strongest AC with FDSI leading by over 2 weeks. For croplands in central and northern India, western China and parts of

22

central plains and mid-west of the U.S. the FDSI -VHI relationship is impacted (reduced AC and longer response-time of VHI) by large-scale irrigation which reduces drought stress due to extreme heat and moisture deficit in the crops (Shah et al., 2021; T. Zhang et al., 2015).
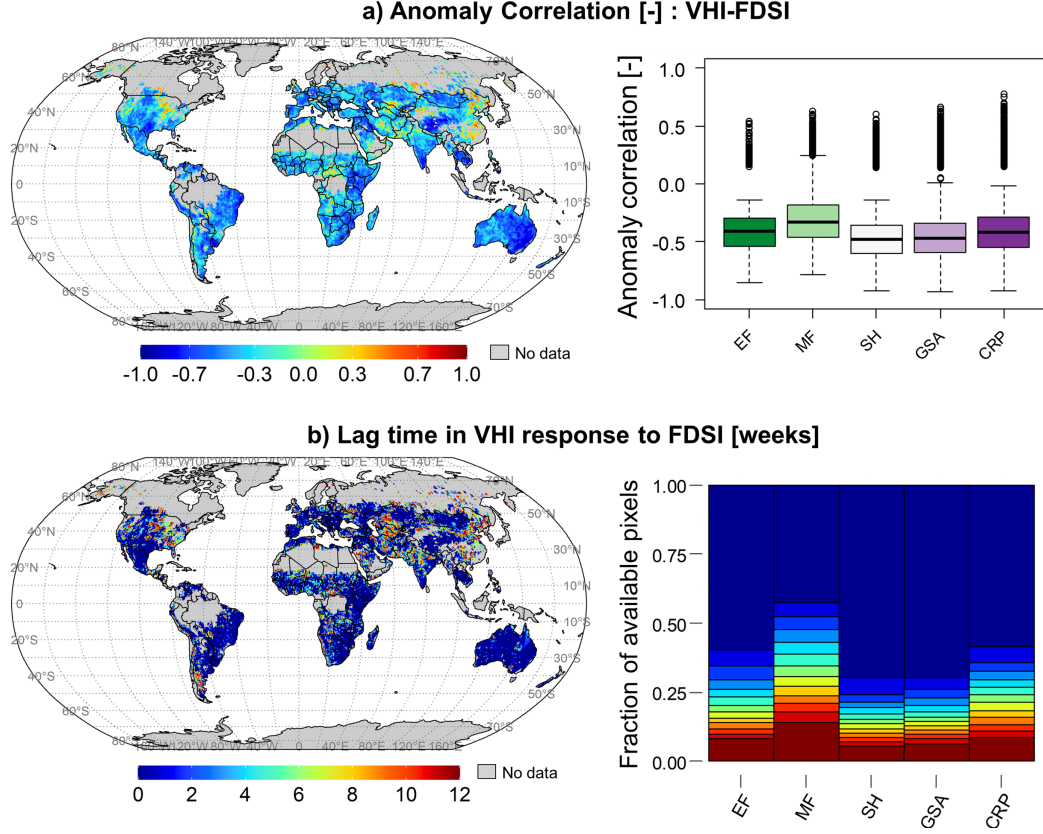
a) Anomaly Correlation [-] : VHI-FDSI

b) Lag time in VHI response to FDSI [weeks]

Figure 10. Global maps and sumary of a) Anomaly correlation [-] between VHI and FDSI and b) Lag time (in weeks) in VHI response to FDSI. Mean-weekly FDSI values are used for the analysis to match the temporal frequency of VHI. Anomaly correlation values with p-value >0.05 are excluded from the analysis. Grey area in the spatial plots indicate pixels with masked/ flagged data. EF= Evergreen forests, MF= Mixed forests, SH= Open or Closed shrublands, GSA= Grasslands and Savannah, CRP= Croplands.

AC between VHI and FDSI is expected to be lower for high-altitude regions and cold/coastal desert ecosystems like Siberia, Mongolia, North-East Canada and Eastern Europe — regions where an increase in temperature can boost vegetative vigor contrary to a key assumption of VHI that an increase in temperature negatively influences vegetation health (Karnieli et al., 2006). It is important to note that the estimates of the pixel-scale θ_{RS} drydown parameters exhibit increased uncertainties over croplands, grasslands and savannah (CGS) ecosystems (for example, in mid-western U.S. and Sahel) during the growing season (Sehgal et al., 2020). This uncertainty is due to a combination of retrieval errors and

complex soil-vegetation-atmospheric dynamics under rapid vegetation growth and irregular/ unknown irrigation not captured by the shallow retrieval depth ($\sim$5 cm) of SMAP. However, active research on improving SMAP retrieval algorithm for heavily vegetated regions and under dense canopies is expected to enhance the retrieval accuracy of θ_{RS} (Colliander et al., 2020), and hence, the accuracy of the drought severity estimates for the CGS ecosystems. Moreover, vegetation can show variable response to the intensity, duration and termination of drought stress based on the type of vegetation (morphology, phenology, root-structure etc.), developmental stage of the plants (Farooq et al., 2009; Lamaoui et al., 2018); and interaction with various meteorological/climatic factors regulated by seasonality and hydro-climate. An evaluation of these complex factors on the relationship between FDSI and VHI is beyond the scope of this study.

5 Summary

This study provides a new methodology for global near-real-time monitoring of flash droughts using two matrices, namely, SMS (drought stress due to SM loss) and RRD (intensification rate of SM loss) derived using SMAP observations. A new index, FDSI, is developed as a non-linear, bivariate function of RRD and SMS to quantify the coupled impact of severity and intensification rate of flash droughts. The proposed matrices are developed using footprint-scale seasonal drydown parameters of θ_{RS} — "*effective*" thresholds of soil hydrologic regimes and land-atmospheric coupling strength. Hence, FDSI is sensitive to the temporal variability in the subgrid-scale land-surface heterogeneity and soil-vegetation-climate interactions. Time invariant SWRPs from PTF, in contrast, lack sensitivity to variabilities in the moderators of SM dynamics at large spatial scales leading to bias/error when used for estimating SMS.

A global assessment shows that FDSI evolves in strong correlation with SPEI-1 with a response time of 0-1 month. Application of FDSI for a mechanistic evaluation of the 2017 flash drought in NGP and retrospective evaluation of select global droughts highlight the reliability of FDSI in capturing emerging and sustained droughts despite limitations of short length of the record (March 2015- March 2019) and shallow penetration depth (0-5 cm). A severity-area-duration assessment of FDSI reveals global drylands as the hotspots of flash droughts on account of high atmospheric moisture demand and stronger land-atmospheric coupling strength in these regions. The study estimates that about 7.8 million km^2 area ($\sim$5% of global landmass) experienced flash drought of 30-50 days duration during 2015-2019. An application of FDSI in forecasting VHI shows promising results for large parts of the globe with high skill in forecasting VHI with up to 2-weeks lead time except over irrigated croplands during growing season, mixed forests and high-altitude deserts.

24

While the study demonstrates a satisfactory application of SMAP for drought monitoring at 36-km resolution, new (and upcoming) dataset from SMAP-Sentinel and SMAP-Enhanced, NASA-ISRO-Synthetic Aperture Radar (NISAR (2018), launch due in 2022) missions provide prospects of extending the proposed approach to finer spatial resolution. Readily available parameters and purely data-driven method facilitates an easy implementation of this study into a real-time, operational framework, advancing global (flash) drought monitoring capabilities.

References

Ajaz, A., Taghvaeian, S., Khand, K., Gowda, P. H., & Moorhead, J. E. (2019). Development and evaluation of an agricultural drought index by harnessing soil moisture and weather data. *Water (Switzerland)*, *11*(7). doi: 10.3390/w11071375

Akbar, R., Short Gianotti, D. J., McColl, K. A., Haghighi, E., Salvucci, G. D., Entekhabi, D., ... Entekhabi, D. (2018). Estimation of landscape soil water losses from satellite observations of soil moisture. *Journal of Hydrometeorology*, *19*(5), 871–889. doi: 10.1175/jhm-d-17-0200.1

Ambika, A. K., & Mishra, V. (2019). Observational evidence of irrigation influence on vegetation health and land surface temperature in india. *Geophysical Research Letters*, *46*(22), 13441–13451. doi: 10.1029/2019GL084367

Bachmair, S., Tanguy, M., Hannaford, J., & Stahl, K. (2018). How well do meteorological indicators represent agricultural and forest drought across europe? *Environmental Research Letters*, *13*(3). doi: 10.1088/1748-9326/aaafda

Bai, J., Cui, Q., Chen, D., Yu, H., Mao, X., Meng, L., & Cai, Y. (2018). Assessment of the smap-derived soil water deficit index (swdi-smap) as an agricultural drought index in

china. *Remote Sensing*, *10*(8). doi: 10.3390/RS10081302

Beguería, S., & Vicente Serrano, S. M. (2020). *Speibase v.2.6 [dataset].* Retrieved from
https://spei.csic.es/database.html doi: http://hdl.handle.net/10261/202305

Beguería, S., Vicente-Serrano, S. M., & Angulo-Martínez, M. (2010). A multiscalar global
drought dataset: The spei base: A new gridded product for the analysis of drought
variability and impacts. *Bulletin of the American Meteorological Society*, *91*(10),
1351–1356. doi: 10.1175/2010BAMS2988.1

Bhuiyan, C., Saha, A. K., Bandyopadhyay, N., & Kogan, F. N. (2017). Analyzing the
impact of thermal stress on vegetation health and agricultural drought–a case study
from gujarat, india. *GIScience and Remote Sensing*, *54*(5), 678–699. doi: 10.1080/
15481603.2017.1309737

Boivin, P. (2011). Shrinkage and swelling phenomena in soils. In *Encyclopedia of earth
sciences series* (Vol. Part 4, pp. 733–735). Springer Netherlands. doi: 10.1007/
978-90-481-3585-1_139

Boivin, P., & Garnier, P. (2004). Relationship between clay content, clay type, and shrinkage
properties of soil samples. *Soil Science Society America Journal*, *68*(July), 1145–1153.
doi: 10.2136/sssaj2004.1145

Burgin, M. S., Colliander, A., Njoku, E. G., Chan, S. K., Cabot, F., Kerr, Y. H., . . . Yueh,
S. H. (2017). A comparative study of the smap passive soil moisture product with
existing satellite-based soil moisture products. *IEEE Transactions on Geoscience and
Remote Sensing*, *55*(5), 2959–2971. doi: 10.1109/TGRS.2017.2656859

Cammalleri, C., Micale, F., & Vogt, J. (2016). A novel soil moisture-based drought severity
index (dsi) combining water deficit magnitude and frequency. *Hydrological processes*,
30(2), 289–301. doi: 10.1002/hyp.10578

Chakraborty, P., Das, B. S., Vasava, H. B., Panigrahi, N., & Santra, P. (2020). Spatial
structure, parameter nonlinearity, and intelligent algorithms in constructing pedo-
transfer functions from large-scale soil legacy data. *Scientific Reports*, *10*(1), 1–13.
doi: 10.1038/s41598-020-72018-2

Chan, S., Bindlish, R., Hunt, R., & Jackson, T. (2013). Ancillary data report for vegetation
water contenet. (047).

Chen, L. G., Gottschalck, J., Hartman, A., Miskus, D., Tinker, R., & Artusa, A. (2019).
Flash drought characteristics based on u.s. drought monitor. *Atmosphere*, *10*(9), 498.
doi: 10.3390/atmos10090498

Chen, Z., Wang, W., & Fu, J. (2020). Vegetation response to precipitation anomalies under
different climatic and biogeographical conditions in china. *Scientific Reports*, *10*(1),
1–16. doi: 10.1038/s41598-020-57910-1

Christian, J. I., Basara, J. B., Hunt, E. D., Otkin, J. A., & Xiao, X. (2020). Flash drought
development and cascading impacts associated with the 2010 russian heatwave. *Envi-
ronmental Research Letters*. doi: 10.1088/1748-9326/ab9faf

Christian, J. I., Basara, J. B., Otkin, J. A., Hunt, E. D., Wakefield, R. A., Flanagan, P. X.,
& Xiao, X. (2019). A methodology for flash drought identification: Application of
flash drought frequency across the united states. *Journal of Hydrometeorology*, *20*(5),
833–846. doi: 10.1175/JHM-D-18-0198.1

Colliander, A., Cosh, M. H., Kelly, V. R., Kraatz, S., Bourgeau-Chavez, L., Siqueira, P.,
. . . Yueh, S. H. (2020). Smap detects soil moisture under temperate forest canopies.
Geophysical Research Letters, *47*(19), 1–10. doi: 10.1029/2020GL089697

Crow, W. T., Berg, A. A., Cosh, M. H., Loew, A., Mohanty, B. P., Panciera, R., . . .
Walker, J. P. (2012). Upscaling sparse ground-based soil moisture observations for the
validation of coarse-resolution satellite soil moisture products. *Reviews of Geophysics*,
50(2). doi: 10.1029/2011RG000372

Dirmeyer, P. A. (2011). The terrestrial segment of soil moisture-climate coupling. *Geophys-
ical Research Letters*, *38*(16), 1–5. doi: 10.1029/2011GL048268

Dong, J., Crow, W., Reichle, R., Liu, Q., Lei, F., & Cosh, M. H. (2019). A global as-
sessment of added value in the smap level 4 soil moisture product relative to its
baseline land surface model. *Geophysical Research Letters*, *46*(12), 6604–6613. doi:

10.1029/2019GL083398

Entekhabi, D., Njoku, E. G., O'Neill, P. E., Kellogg, K. H., Crow, W. T., Edelstein, W. N., ... Van Zyl, J. (2010). The soil moisture active passive (smap) mission. *Proceedings of the IEEE*, *98*(5), 704–716. doi: 10.1109/JPROC.2010.2043918

Farooq, M., Wahid, A., Kobayashi, N., Fujita, D., & Basra, S. M. A. (2009). Plant drought stress: effects, mechanisms and management. In *Sustainable agriculture* (pp. 153–188). Springer.

Gaur, N., & Mohanty, B. P. (2013). Evolution of physical controls for soil moisture in humid and subhumid watersheds. *Water Resources Research*, *49*(3), 1244–1258. doi: 10.1002/wrcr.20069

Gaur, N., & Mohanty, B. P. (2016). Land-surface controls on near-surface soil moisture dynamics: Traversing remote sensing footprints. *Water Resources Research*, *52*(8), 6365–6385. doi: 10.1002/2015WR018095

Gaur, N., & Mohanty, B. P. (2019). A nomograph to incorporate geophysical heterogeneity in soil moisture downscaling. *Water Resources Research*, *55*(1), 34–54. doi: 10.1029/2018WR023513

Gitelson, A. A., Kogan, F., Zakarin, E., Spivak, L., & Lebed, L. (1998). Using avhrr data for quantitive estimation of vegetation conditions: Calibration and validation. *Advances in Space Research*, *22*(5), 673–676.

Grossiord, C., Sevanto, S., Adams, H. D., Collins, A. D., Dickman, L. T., McBranch, N., ... McDowell, N. G. (2017). Precipitation, not air temperature, drives functional responses of trees in semi-arid ecosystems. *Journal of Ecology*, *105*(1), 163–175.

Hester, M. W., Willis, J. M., Rouhani, S., Steinhoff, M. A., & Baker, M. C. (2016). Impacts of the deepwater horizon oil spill on the salt marsh vegetation of louisiana. *Environmental Pollution*, *216*, 361–370. doi: 10.1016/j.envpol.2016.05.065

Hirschi, M., Mueller, B., Dorigo, W., & Seneviratne, S. I. (2014). Using remotely sensed soil moisture for land-atmosphere coupling diagnostics: The role of surface vs. root-zone soil moisture variability. *Remote Sensing of Environment*, *154*, 246–252. doi: 10.1016/j.rse.2014.08.030

Hodnett, M. G., & Tomasella, J. (2002). Marked differences between van genuchten soil water-retention parameters for temperate and tropical soils: A new water-retention pedo-transfer functions developed for tropical soils. *Geoderma*, *108*(3-4), 155–180. doi: 10.1016/S0016-7061(02)00105-2

Hunt, E. D., Hubbard, K. G., Wilhite, D. A., Arkebauer, T. J., & Dutcher, A. L. (2009). The development and evaluation of a soil moisture index. *International Journal of Climatology*, *29*(5), 747–759. doi: 10.1002/joc.1749

Jackson, T., O'Neill, P., Chan, S., Bindlish, R., Colliander, A., Chen, F., & Dunbar, S. (2018). *Soil moisture active passive (smap) project: Calibration and validation for the l2/3$_s$m$_p$version5andl2/3$_s$m$_{pe}$version2dataproductscitation* (*Tech. Rep.*).

James, S. E., Pärtel, M., Wilson, S. D., & Peltzer, D. A. (2003). Temporal heterogeneity of soil moisture in grassland and forest. *Journal of Ecology*, *91*(2), 234–239. doi: 10.1046/j.1365-2745.2003.00758.x

Jencso, K., Parker, B., Rath, M., Syner, M., Fuchs, B., Johnson, S., ... Sage, J. (2019). *Lessons learned from the 2017 drought across* (Tech. Rep.).

Jin, C., Luo, X., Xiao, X., Dong, J., Li, X., Yang, J., & Zhao, D. (2019). The 2012 flash drought threatened us midwest agroecosystems. *Chinese Geographical Science*, *29*(5), 768–783. doi: 10.1007/s11769-019-1066-7

Karnieli, A., Bayasgalan, M., Bayarjargal, Y., Agam, N., Khudulmur, S., & Tucker, C. J. (2006). Comments on the use of the vegetation health index over mongolia. *International journal of remote sensing*, *27*(10), 2017–2024. doi: 10.1080/01431160500121727

Kogan, F. (1997). Global drought watch from space. *Bulletin of the American Meteorological Society*, *78*(4), 621–636. doi: 10.1175/1520-0477(1997)078{\textless}0621: GDWFS{\textgreater}2.0.CO;2

Kogan, F. (2002). World droughts in the new millennium from avhrr-based vegetation

health indices. *Eos, Transactions American Geophysical Union*, *83*(48), 557. doi: 10.1029/2002EO000382

Kogan, F. (2018). Space-based vegetation health for wheat yield modeling and prediction in australia. *Journal of applied remote sensing*, *12*(02), 1. doi: 10.1117/1.JRS.12.026002

Kogan, F., Salazar, L., & Roytman, L. (2012). Forecasting crop production using satellite-based vegetation health indices in kansas, usa. *International Journal of Remote Sensing*, *33*(9), 2798–2814. doi: 10.1080/01431161.2011.621464

Kolassa, J., Reichle, R. H., Liu, Q., Alemohammad, S. H., Gentine, P., Aida, K., ... Walker, J. P. (2018). Estimating surface soil moisture from smap observations using a neural network technique. *Remote Sensing of Environment*, *204*, 43–59. doi: 10.1016/j.rse.2017.10.045

Koster, R. D., Crow, W. T., Reichle, R. H., & Mahanama, S. P. (2018). Estimating basin-scale water budgets with smap soil moisture data. *Water Resources Research*, *54*(7), 4228–4244. doi: 10.1029/2018WR022669

Laio, F., Porporato, A., Fernandez-Illescas, C. P., & Rodriguez-Iturbe, I. (2001). Plants in water-controlled ecosystems: Active role in hydrologic processes and responce to water stress iv. discussion of real cases. *Advances in Water Resources*, *24*(7), 745–762. doi: 10.1016/S0309-1708(01)00007-0

Lamaoui, M., Jemo, M., Datla, R., & Bekkaoui, F. (2018). Heat and drought stresses in crops and approaches for their mitigation. *Frontiers in Chemistry*, *6*(February), 1–14. doi: 10.3389/fchem.2018.00026

Lambin, E. F., & Ehrlich, D. (1996). The surface temperature-vegetation index space for land cover and land-cover change analysis. *International journal of remote sensing*, *17*(3), 463–487. doi: 10.1080/01431169608949021

Lawston, P. M., Santanello, J. A., & Kumar, V. S. (2017). Irrigation signals detected from smap soil moisture retrievals. *Geophysical Research Letters*, *44*(23), 11,860–11,867. doi: 10.1002/2017GL075733

Liu, Mishra, A. K., Yu, Z., Yang, C., Konapala, G., & Vu, T. (2017). Performance of smap, amsr-e and lai for weekly agricultural drought forecasting over continental united states. *Journal of Hydrology*, *553*, 88–104. doi: 10.1016/j.jhydrol.2017.07.049

Liu, Zhu, Y., Zhang, L., Ren, L., Yuan, F., Yang, X., & Jiang, S. (2020). Flash droughts characterization over china: From a perspective of the rapid intensification rate. *Science of the Total Environment*, *704*, 135373. doi: 10.1016/j.scitotenv.2019.135373

Liu, Y., Zhu, Y., Ren, L., Otkin, J., Hunt, E. D., Yang, X., ... Jian, S. (2020). Two different methods for flash drought identification: Comparison of their strengths and limitations. *Journal of Hydrometeorology*, *21*(4), 691–704. doi: 10.1175/JHM-D-19-0088.1

Mahto, S. S., & Mishra, V. (2020). Dominance of summer monsoon flash droughts in india. *Environmental Research Letters*. doi: 10.1088/1748-9326/abaf1d

Martínez-Fernández, J., González-Zamora, A., Sánchez, N., & Gumuzzio, A. (2015). A soil water based index as a suitable agricultural drought indicator. *Journal of Hydrology*, *522*, 265–273.

Martínez-Fernández, J., González-Zamora, A., Sánchez, N., Gumuzzio, A., & Herrero-Jiménez, C. (2016). Satellite soil moisture for agricultural drought monitoring: Assessment of the smos derived soil water deficit index. , *177*, 277–286.

McColl, K. A., Wang, W., Peng, B., Akbar, R., Short Gianotti, D. J., Lu, H., ... Entekhabi, D. (2017). Global characterization of surface soil moisture drydowns. *Geophysical Research Letters*, *44*(8), 3682–3690. doi: 10.1002/2017GL072819

Mishra, A., Vu, T., Veettil, A. V., & Entekhabi, D. (2017). Drought monitoring with soil moisture active passive (smap) measurements. *Journal of Hydrology*, *552*, 620–632. doi: 10.1016/j.jhydrol.2017.07.033

Mladenova, I. E., Bolten, J. D., Crow, W. T., Sazib, N., Cosh, M. H., Tucker, C. J., & Reynolds, C. (2019). Evaluating the operational application of smap for global agricultural drought monitoring. *IEEE Journal of Selected Topics in Applied Earth Observations and Remote Sensing*, *12*(9), 3387–3397. doi: 10.1109/jstars.2019.2923555

28

Mo, K. C., & Lettenmaier, D. P. (2015). Heat wave flash droughts in decline. *Geophysical Research Letters*, *42*(8), 2823–2829. doi: 10.1002/2015GL064018

Mo, K. C., & Lettenmaier, D. P. (2016). Precipitation deficit flash droughts over the united states. *Journal of Hydrometeorology*, *17*(4), 1169–1184. doi: 10.1175/JHM-D-15-0158 .1

Mo, K. C., & Plettenmaier, D. (2020). Prediction of flash droughts over the united states. *Journal of Hydrometeorology*, *21*(8), 1793–1810. doi: 10.1175/JHM-D-19-0221.1

Mozny, M., Trnka, M., Zalud, Z., Hlavinka, P., Nekovar, J., Potop, V., & Virag, M. (2012). Use of a soil moisture network for drought monitoring in the czech republic. *Theoretical and Applied Climatology*, *107*(1-2), 99–111. doi: 10.1007/s00704-011-0460-6

Nachtergaele, F., Van Velthuizen, H., Verelst, L., Batjes, N., Dijkshoorn, K., Van Engelen, V., . . . Shi, X. (2012). *Harmonized world soil database - version 1.2* (Tech. Rep.).

Nguyen, H., Wheeler, M. C., Otkin, J. A., Cowan, T., Frost, A., & Stone, R. (2019). Using the evaporative stress index to monitor flash drought in australia. *Environmental Research Letters*, *14*(6). doi: 10.1088/1748-9326/ab2103

NISAR. (2018). Nasa-isro sar (nisar) mission science users' handbook. *California Institute of technology, Jet Propulsion Laboaroty*(January), 261.

Noguera, I., Domínguez-Castro, F., & Vicente-Serrano, S. M. (2020). Characteristics and trends of flash droughts in spain, 1961–2018. *Annals of the New York Academy of Sciences*, *1472*(1), 155–172. doi: 10.1111/nyas.14365

O'Neill. (2018). *Smap l3 radiometer global daily 36 km ease-grid soil moisture, version 5* (Tech. Rep.). doi: https://doi.org/10.5067/ZX7YX2Y2LHEB

Osman, M., Zaitchik, B. F., Badr, H. S., Christian, J. I., Tadesse, T., Otkin, J. A., & Anderson, M. C. (2020). Flash drought onset over the contiguous united states: Sensitivity of inventories and trends to quantitative definitions. *Hydrology and Earth System Sciences Discussions*, *In review*. doi: 10.5194/hess-2020-385

Otkin, J. A., Svoboda, M., Hunt, E. D., Ford, T. W., Anderson, M. C., Hain, C., & Basara, J. B. (2017). Flash droughts: a review and assessment of the challenges imposed by rapid onset droughts in the united states. *Bulletin of the American Meteorological Society*. doi: 10.1175/BAMS-D-17-0149.1

Otkin, J. A., Svoboda, M., Hunt, E. D., Ford, T. W., Anderson, M. C., Hain, C., & Basara, J. B. (2018). Flash droughts: A review and assessment of the challenges imposed by rapid-onset droughts in the united states. *Bulletin of the American Meteorological Society*, *99*(5), 911–919. doi: 10.1175/BAMS-D-17-0149.1

Pablos, M., González-Zamora, , Sánchez, N., & Martínez-Fernández, J. (2018). Assessment of root zone soil moisture estimations from smap, smos and modis observations. *Remote Sensing*, *10*(7). doi: 10.3390/rs10070981

Pachepsky, Y. A., & van Genuchten, M. T. (2011). Pedotransfer functions. In J. Gliński, J. Horabik, & J. Lipiec (Eds.), *Encyclopedia of agrophysics* (pp. 556–561). Dordrecht: Springer Netherlands. doi: 10.1007/978-90-481-3585-1_109

Pendergrass, A. G., Meehl, G. A., Pulwarty, R., Hobbins, M., Hoell, A., AghaKouchak, A., . . . Woodhouse, C. A. (2020). Flash droughts present a new challenge for subseasonal-to-seasonal prediction. *Nature Climate Change*, *10*(3), 191–199. doi: 10.1038/s41558 -020-0709-0

Peña-Gallardo, M., Vicente-Serrano, S. M., Hannaford, J., Lorenzo-Lacruz, J., Svoboda, M., Domínguez-Castro, F., . . . Kenawy, E. A. (2019). Complex influences of meteorological drought time-scales on hydrological droughts in natural basins of the contiguous unites states. *Journal of Hydrology*, *568*(July 2018), 611–625. doi: 10.1016/j.jhydrol.2018 .11.026

Pollacco, J. A., & Mohanty, B. P. (2012). Uncertainties of water fluxes in soil-vegetation-atmosphere transfer models: Inverting surface soil moisture and evapotranspiration retrieved from remote sensing. *Vadose Zone Journal*, *11*(3). doi: 10.2136/vzj2011 .0167

Pribyl, D. W. (2010). A critical review of the conventional soc to som conversion factor. *Geoderma*. doi: 10.1016/j.geoderma.2010.02.003

Purdy, A. J., Fisher, J. B., Goulden, M. L., Colliander, A., Halverson, G., Tu, K., & Famiglietti, J. S. (2018). Smap soil moisture improves global evapotranspiration. *Remote Sensing of Environment*, *219*(September), 1–14. doi: 10.1016/j.rse.2018.09.023

Reichle, R. H., de Lannoy, G. J., Liu, Q., Koster, R. D., Kimball, J. S., Crow, W. T., ... Smith, E. B. (2017). Global assessment of the smap level-4 surface and root-zone soil moisture product using assimilation diagnostics. *Journal of Hydrometeorology*, *18*(12), 3217–3237. doi: 10.1175/JHM-D-17-0130.1

Reichle, R. H., De Lannoy, G. J. M., Liu, Q., Colliander, A., Conaty, A., Jackson, T., ... Koster, R. D. (2015). *Technical report series on global modeling and data assimilation, volume 40 soil moisture active passive (smap) project assessment report for the beta-release l4_s m data product* (*Vol. 40; Tech. Rep.*).

Reichle, R. H., Draper, C. S., Liu, Q., Girotto, M., Mahanama, S. P., Koster, R. D., & De Lannoy, G. J. (2017). Assessment of merra-2 land surface hydrology estimates. *Journal of Climate*, *30*(8), 2937–2960. doi: 10.1175/JCLI-D-16-0720.1

Rodriguez-Iturbe, I. (2000). Ecohydrology: A hydrologic perspective of climate-soil-vegetation dynamics. *Water Resources Research*, *36*(1), 3–9. doi: 10.1029/1999WR900210

Rodriguez-Iturbe, I., Porporato, A., Rldolfi, L., Isham, V., & Cox, D. R. (1999). Probabilistic modelling of water balance at a point: The role of climate, soil and vegetation. *Proceedings of the Royal Society A: Mathematical, Physical and Engineering Sciences*, *455*(1990), 3789–3805. doi: 10.1098/rspa.1999.0477

Sadeghi, M., Ebtehaj, A., Crow, W. T., Gao, L., Purdy, A. J., Fisher, J. B., ... Tuller, M. (2020). Global estimates of land surface water fluxes from smos and smap satellite soil moisture data. *Journal of Hydrometeorology*, *21*(2), 241–253. doi: 10.1175/JHM-D-19-0150.1

Sadri, S., Pan, M., Wada, Y., Vergopolan, N., Sheffield, J., Famiglietti, J. S., ... Wood, E. (2020). Remote sensing of environment a global near-real-time soil moisture index monitor for food security using integrated smos and smap. *Remote Sensing of Environment*, *246*(April), 111864. doi: 10.1016/j.rse.2020.111864

Sadri, S., Wood, E. F., & Pan, M. (2018). Developing a drought-monitoring index for the contiguous us using smap. *Hydrology and Earth System Sciences*, *22*(12), 6611–6626. doi: 10.5194/hess-22-6611-2018

Sahoo, S., Dhar, A., Debsarkar, A., Kar, A., & Kayet, N. (2020). Identification of water-stressed area based on the interrelationship of soil moisture and seasonal rice cultivation. *Paddy and Water Environment*, *18*(1), 193–209. doi: 10.1007/s10333-019-00774-7

Santra, P., Kumar, M., Kumawat, R. N., Painuli, D. K., Hati, K. M., Heuvelink, G. B., & Batjes, N. H. (2018). Pedotransfer functions to estimate soil water content at field capacity and permanent wilting point in hot arid western india. *Journal of Earth System Science*, *127*(3), 1–16. doi: 10.1007/s12040-018-0937-0

Saxton, K. E., & Rawls, W. J. (2006). Soil water characteristic estimates by texture and organic matter for hydrologic solutions. *Soil Science Society of America Journal*, *70*(5), 1569–1578. doi: 10.2136/sssaj2005.0117

Schwalm, C. R., Anderegg, W. R. L., Michalak, A. M., Fisher, J. B., Biondi, F., Koch, G., ... Tian, H. (2017). Global patterns of drought recovery. *Nature*, *548*(7666), 202–205. doi: 10.1038/nature23021

Sehgal, V., Gaur, N., & Mohanty, B. P. (2020). Global surface soil moisture drydown patterns. *Water Resources Research*, *57*(1). doi: 10.1029/2020WR027588

Sehgal, V., & Sridhar, V. (2019). Watershed-scale retrospective drought analysis and seasonal forecasting using multi-layer, high-resolution simulated soil moisture for southeastern u.s. *Weather and Climate Extremes*, *23*, 100191. doi: 10.1016/j.wace.2018.100191

Sehgal, V., Sridhar, V., & Tyagi, A. (2017). Stratified drought analysis using a stochastic ensemble of simulated and in-situ soil moisture observations. *Journal of Hydrology*,

545, 226–250. doi: 10.1016/j.jhydrol.2016.12.033

Shah, D., Shah, H. L., Dave, H. M., & Mishra, V. (2021). Contrasting influence of human activities on agricultural and hydrological droughts in india. *Science of The Total Environment*, 144959. doi: 10.1016/j.scitotenv.2021.144959

Shangguan, W., Dai, Y., Duan, Q., Liu, B., & Yuan, H. (2014). A global soil data set for earth system modeling. *Journal of Advances in Modeling Earth Systems*, *6*(1), 249–263. doi: 10.1002/2013MS000293

Skaggs, T. H., Anderson, R. G., Corwin, D. L., & Suarez, D. L. (2014). Analytical steady-state solutions for water-limited cropping systems using saline irrigation water. *Water Resources Research*, *50*(12), 9656–9674. doi: 10.1002/2014WR016058

Skaggs, T. H., van Genuchten, M. T., Shouse, P. J., & Poss, J. A. (2006). Macroscopic approaches to root water uptake as a function of water and salinity stress. *Agricultural Water Management*, *86*(1-2), 140–149. doi: 10.1016/j.agwat.2006.06.005

Sridhar, V., Hubbard, K. G., You, J., & Hunt, E. D. (2008). Development of the soil moisture index to quantify agricultural drought and its "user friendliness" in severity-area-duration assessment.
doi: 10.1175/2007JHM892.1

Touma, D., Ashfaq, M., Nayak, M. A., Kao, S.-C. C., & Diffenbaugh, N. S. (2015). A multi-model and multi-index evaluation of drought characteristics in the 21st century. *Journal of hydrology*, *526*, 196–207. doi: 10.1016/j.jhydrol.2014.12.011

UNEP. (1997). *World atlas of desertification* (Tech. Rep.). London ;. 1997. (Bibliography: p. 171-180.)

van Genuchten, M. (1987). *A numerical model for water and solute movement* (Tech. Rep.). Riverside, CA.

van Genuchten, M., & Gupta, S. (1993). A reassessment of the crop tolerance response function. *Journal of the Indian Society of Soil Science*, *41*(4), 730–737.

van Straten, G., de Vos, A. C., Rozema, J., Bruning, B., & van Bodegom, P. M. (2019). An improved methodology to evaluate crop salt tolerance from field trials. *Agricultural Water Management*, *213*(August 2018), 375–387. doi: 10.1016/j.agwat.2018.09.008

Vicente-Serrano, S. M., Beguería, S., Lorenzo-Lacruz, J., Camarero, J. J., López-Moreno, J. I., Azorin-Molina, C., ... Sanchez-Lorenzo, A. (2012). Performance of drought indices for ecological, agricultural, and hydrological applications. *Earth Interactions*, *16*(10), 1–27.

Vicente-Serrano, S. M., Beguería, S., & López-Moreno, J. I. (2010). A multiscalar drought index sensitive to global warming: The standardized precipitation evapotranspiration index. *Journal of climate*, *23*(7), 1696–1718. doi: 10.1175/2009JCLI2909.1

Western, A. W., Grayson, R. B., Blöschl, G., & Wilson, D. J. (2003). Spatial variability of soil moisture and its implications for scaling. *Scaling methods in soil physics*, 119–142.

Wu, B., Ma, Z., & Yan, N. (2020). Agricultural drought mitigating indices derived from the changes in drought characteristics. *Remote Sensing of Environment*, *244*(March), 111813. doi: 10.1016/j.rse.2020.111813

Yuan, X., Wang, L., Wu, P., Ji, P., Sheffield, J., & Zhang, M. (2019). Anthropogenic shift towards higher risk of flash drought over china. *Nature Communications*, *10*(1), 1–8. doi: 10.1038/s41467-019-12692-7

Zhang, Q., Kong, D., Singh, V. P., & Shi, P. (2017). Response of vegetation to different time-scales drought across china: Spatiotemporal patterns, causes and implications. *Global and Planetary Change*, *152*, 1–11. doi: 10.1016/j.gloplacha.2017.02.008

Zhang, T., Lin, X., & Sassenrath, G. F. (2015). Current irrigation practices in the central united states reduce drought and extreme heat impacts for maize and soybean, but not for wheat. *Science of the Total Environment*, *508*, 331–342.

Zhang, X., Zhao, W., Liu, Y., Fang, X., & Feng, Q. (2016). The relationships between grasslands and soil moisture on the loess plateau of china: A review. *Catena*, *145*, 56–67. doi: 10.1016/j.catena.2016.05.022

Zhao, M., A, G., Velicogna, I., & Kimball, J. S. (2017). A global gridded dataset of grace drought severity index for 2002–14: Comparison with pdsi and spei and a case study

of the australia millennium drought. *Journal of Hydrometeorology*, *18*(8), 2117–2129. doi: 10.1175/JHM-D-16-0182.1

Zhao, T., Liu, P., Zhang, Y., & Ruan, C. (2017). Relating anomaly correlation to lead time: Clustering analysis of cfsv2 forecasts of summer precipitation in china. *Journal of Geophysical Research: Atmospheres*, *122*(17), 9094–9106. doi: 10.1002/2017JD027018

Zhao, T., Zhang, Y., & Chen, X. (2019). Predictive performance of nmme seasonal forecasts of global precipitation: A spatial-temporal perspective. *Journal of Hydrology*, *570*(January), 17–25. doi: 10.1016/j.jhydrol.2018.12.036

Ziese, M., Schneider, U., Meyer-Christoffer, A., Schamm, K., Vido, J., Finger, P., . . . Becker, A. (2014). The gpcc drought index – a new, combined and gridded global drought index. *Earth System Science Data*, *6*(2), 285–295. doi: 10.5194/essd-6-285-2014

Zscheischler, J., Orth, R., & Seneviratne, S. I. (2015). A submonthly database for detecting changes in vegetation-atmosphere coupling. *Geophysical Research Letters*, *42*(22), 9816–9824. doi: 10.1002/2015GL066563